January 2016

ULTRA SHORT PULSE LASER SURFACE MODIFICATION

Shashank Sarbada
Purdue University

Follow this and additional works at: https://docs.lib.purdue.edu/open_access_theses

PURDUE UNIVERSITY
GRADUATE SCHOOL
Thesis/Dissertation Acceptance

This is to certify that the thesis/dissertation prepared

By _Shashank Sarbada_

Entitled
ULTRA SHORT PULSE LASER SURFACE MODIFICATION

For the degree of _Master of Science in Mechanical Engineering_

Is approved by the final examining committee:

Yung C. Shin
_____
Chair

Fu Zhao

Peter Bermel

To the best of my knowledge and as understood by the student in the Thesis/Dissertation Agreement, Publication Delay, and Certification Disclaimer (Graduate School Form 32), this thesis/dissertation adheres to the provisions of Purdue University's "Policy of Integrity in Research" and the use of copyright material.

Approved by Major Professor(s): _Yung C. Shin_

Approved by: _Jay P. Gore_   12/2/2016

Head of the Departmental Graduate Program   Date

ULTRA SHORT PULSE LASER SURFACE MODIFICATION

A Thesis

Submitted to the Faculty

of

Purdue University

by

Shashank Sarbada

In Partial Fulfillment of the

Requirements for the Degree

of

Master of Science in Mechanical Engineering

December 2016

Purdue University

West Lafayette, Indiana

Dedicated to my family

ACKNOWLEDGEMENTS

TABLE OF CONTENTS

Page

LIST OF TABLES

LIST OF FIGURES

ABSTRACT

Sarbada, Shashank. M.S.M.E., Purdue University, December 2016. Ultra Short Pulse Laser Surface Modification. Major Professor: Yung C. Shin, School of Mechanical Engineering.

Surface structure plays an important role in determining the nature of interactions between materials and their surroundings. The optical, mechanical, thermal and other physical properties of surfaces can be modified and controlled through the careful design of the surface structure. Although there are several methods to modify surfaces to achieve the desired properties, each of these methods has certain limitations associated with it. In this thesis, ultra-short pulse femtosecond and picosecond lasers have been used to create surface structures on various materials to achieve desired surface properties. The advantages of using ultra-short pulse lasers for surface modification over other commonly used techniques have been highlighted.

The first part of the thesis deals with the enhancement of the optical properties of solar cell surfaces. A picosecond laser is used to create nanostructures on the surface of silicon to modify the surface reflectance and improve the light trapping efficiency of solar cells. The effects of varying process parameters such as laser fluence, scan speed, overlapping ratio and polarization angle on the formation of surface structures are reported. The experimental results are compared with finite difference time domain

(FDTD) simulations and are in good agreement, showing high predictably in reflectance values for different surface structures.

In the next part of the thesis, the effects of surface structures on the wettability of surfaces are discussed. A femtosecond laser is used to create superhydrophobic surface structures on metal surfaces. A process to transfer surface structures from metal surfaces to polymers is demonstrated resulting in superhydrophobic polymer surfaces. Various surface micro and nanostructures are presented and their wetting properties are discussed. A fast and inexpensive method to create microfluidic devices with textured superhydrophobic inner channel walls is also presented. These channels allow a controllable fluid flow rate through microfluidic devices fabricated by taking advantage of the transferability of superhydrophobic surfaces onto polymers.

CHAPTER 1. INTRODUCTION

1.1   Motivation

Surface texturing at the micro scale has been demonstrated using many techniques over the past century. These methods include chemical etching, mechanical scribing, physical deposition, laser processing, reactive ion etching and several others. These modified surfaces have been used in many fields of engineering such as tribology, optics, metrology, electronics, and biology among others. Each texturing technique has certain advantages and limitations, which determine its suitability for an engineering application.

Conventional surface texturing techniques such as mechanical scribing and milling are limited by the size of tools available. As the scale of the desired surface features reduces down to the micro scale, it becomes increasingly difficult to manufacture tools that can create these surface features. Complex surface geometries require the use of specialized tools which are expensive to manufacture. Micro tools also tend to wear rapidly and as a result have a short tool life. The range of parameters within which these micro tools function optimally is narrow and this limits the speeds of surface texturing. As a result, mechanical scribing is not suitable for texturing large areas. In addition to this, certain materials such as abrasive ceramics and materials harder than the tool cannot be textured easily using these techniques. Therefore, there are several limitations to using mechanical scribing and milling for large scale surface texturing.

Chemical and electrochemical etching processes are widely used and are capable of producing micro and nano scale roughness on surfaces. However, precise control of surface features is difficult to achieve with these methods. Well defined geometrical features are difficult to produce repeatably over large areas. Different materials require different chemical etchants, making the process limited to specific materials. The storage and disposal of chemical etchants is also expensive and often hazardous to the user and the environment.

Methods such as focused ion beam milling and electron beam machining allow high precision down to the nano scale but are limited to small features. These methods are slow and are not scalable to large production. Lithography is a tool which is widely used to produce detailed micro and nano scale features on surfaces. However, the process involves multiple steps and requires the use of chemicals. It also requires a clean environment to prevent contamination that can negatively affect the process. Conventional laser scribing, using continuous wave (CW) lasers and micro to nano second pulsed lasers, is commonly used to produce micro scale features at high processing speeds on a wide range of materials. These lasers allow texturing of large areas with high reproducibility. The drawback of these laser systems arises due to the unwanted thermal effects of longer pulse widths and CW lasers which cause melting of materials and surface oxidation. These lasers are not ideal for the creation of sub-micron surface features.

Although several methods exist to modify surface features for engineering applications, the emergence of new technologies provides an opportunity to improve existing processes and establish new ones. With the rapid growth in the field of ultra-

short pulse lasers over the past decade, new opportunities have emerged to improve surface texturing at the micro and nano scale. These lasers allow precise control of surface features at high processing speeds. The development of robust laser systems has allowed the adoption of these high precision systems in industrial applications. With the proper design of experiments and selection of process parameters, several engineering applications can be improved and made more efficient with the use of ultra-short pulse lasers. Two such applications are identified and serve as the motivation for this work.

With the growing need for renewable energy sources, there is an increasing demand for cheap and high efficiency solar cells. Although high efficiency silicon solar cells with overall efficiencies over 25% [1] have been fabricated in laboratories, the high cost involved in manufacturing these high efficiency devices makes their commercial use impractical. Optical losses through front surface reflections lower the overall efficiency of solar cells since bare silicon reflects nearly 40% of incident solar radiation over the wavelength range of 200 nm to 1100 nm. Laser surface texturing is a technique used to minimize these optical losses thus increasing solar cell efficiency. By determining the optimal surface structures for light trapping and by optimizing process parameters of laser surface texturing of solar cells, high processing speeds required in industrial production can be achieved. This is meant to serve as an alternative to conventional anti-reflective coatings (ARCs) which involve slow and expensive manufacturing processes.

Surface texturing to create superhydrophobic surfaces has been a topic of interest for many researchers over the last few decades. Microfluidics is one field in which superhydrophobicity can play a pivotal role. The control of fluid flow through microfluidic devices is essential in many applications. Accurately controlling fluid flow

in these devices using surface texturing is challenging due to the small length scales involved and the lack of a good fabrication technique. Laser surface texturing is one potential technique to create superhydrophobic surfaces that can be used to manipulate fluid flow. This area needs to be further explored and is a motivation for this work.

In the next few sections, these two applications of textured surface will be discussed in detail and the advantages of using laser surface texturing in these applications will be highlighted.

1.2 Background Information

1.2.1 Laser surface texturing

Laser surface texturing is a widely used method to produce micro and nano scale features on a wide variety of materials for a host of applications. Laser surface texturing has several advantages over other commonly used surface texturing methods. These advantages over conventional techniques such as machining and chemical etching include high dimensional accuracy, ability to create detailed structures down to the sub-micron scale, high processing speed and repeatability. In addition to this, laser processing does not require the use of chemicals and other consumables and does not generate waste.

There has been a gradual shift in the scale of laser textured surface features reported in literature from micro to nano scale. This has been accompanied by a shift from longer pulse lasers and continuous wave lasers to short and ultra-short pulse lasers. Laser surface texturing to enhance material surface properties has been reported in literature since the 1990s. Some of the earliest reports of laser surface texturing for

surface property enhancement were aimed at improving the tribological performance of materials. Baumgart et al. [2] used an Nd:YLF nano second laser to create surface micro bumps on magnetic disc drives to improve tribological performance while Geiger et al. [3] used an excimer laser to create microstructures to improve the tribological behavior of ceramics. Etison et al. [4] improved mechanical seal performance by creating microstructures using laser surface texturing. In the early 2000s, laser surface texturing was reported to be used to reduce wear in metals [5] and to improve the tool life of forging dies [6]. Over the last decade there have been more studies reporting the enhancement of tribological properties using laser surface texturing [7,8], most of which were focused on creating micro scale features. More recently however, nano scale surface features have been utilized to improve tribological properties of surfaces created using ultra-short pulsed femtosecond and picosecond lasers, as reported by Bonse et al. [9] and Wang et al. [10]. This gradual shift towards ultra-short pulse lasers is due to the inherent advantages ultra-short pulse widths have over continuous wave (CW) and longer pulse width lasers. The pulse durations of ultra-short pulse lasers are shorter than the thermal diffusion time in materials ensuring minimum thermal damage, thus allowing cold ablation of material. Due to the high power density of ultra-short pulses the material is directly sublimated to plasma with negligible thermal debris. This creates highly localized interactions allowing high precision material processing.

During the last decade there have also been a number of studies aimed at improving the optical and wetting properties of surfaces which will be discussed in greater detail in subsequent sections.

1.2.2   Picosecond laser induced periodic surface structures

Laser induced periodic surface structures (LIPSS), as the name suggests, are grating like structures with a periodic spacing commonly observed on surfaces irradiated with lasers. Ripple structures having a period nearly equal to the wavelength of incident radiation are commonly referred to as low special frequency LIPSS (LSFL) and are formed orthogonal to the direction of the polarization of the laser. LIPSS with periods significantly shorter than the wavelength of the laser have also been commonly reported in literature and are formed when ultra-short pulsed lasers are used. These are known as high special frequency LIPSS (HSFL) and are oriented parallel or perpendicular to the direction of polarization. Figure 1-1 shows these two different type of LIPSS created on stainless steel using a femtosecond laser. The periodicity P of LIPSS is approximately given by the Equation (1.1).

$$P = \frac{\lambda}{Re[\eta] \pm Sin\theta} \ \ with \ g \ || \ E_t \qquad\qquad (1.1)$$

where λ is the incident light wavelength, $\eta = \varepsilon_{air} \ \varepsilon_{material}/(\varepsilon_{air} \ \varepsilon_{material})^{1/2}$ is the effective refractive index of the air–material interface with $\varepsilon_{air} \ and \ \varepsilon_{material}$ being the dielectric constants of air and the material, $Re \ [\eta]$ is the real part of $[\eta]$, θ is the beam incident angle, g is the grating vector of LIPSS, and E_t is the tangential component of electric field vector of the incident wave [11]. However, factors such as the number of pulses per spot also affect the LIPSS period and some modifications of this equation have been reported in literature [12].
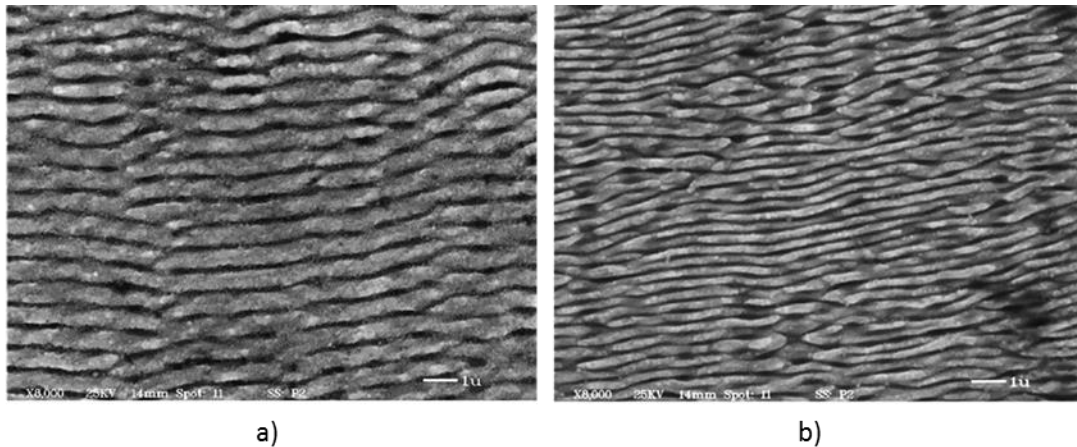
Figure 1-1. a) Low spatial frequency LIPSS and, b) High spatial frequency LIPSS, created on stainless steel using femtosecond laser pulses.

There have been many theories regarding the formation of LIPSS. The formation of LSFL was earlier attributed to the interference between the incident laser radiation and the surface scattered waves but was later improved by the efficacy factor theory of Sipe et al. [13]. The theory explains that LIPSS are formed due to inhomogeneous energy absorption just beneath the surface, induced by surface roughness. The incident laser pulse causes carrier generation in the conduction band, which transiently changes the optical properties of the sample. This transient change of the optical properties leads to the excitation of surface plasmon polaritons, which interfere with the incident laser beam and then leads to a modulated energy deposition into the material. The formation of HSFL is still not fully explained but has been attributed to the redistribution of the electric field over the surface due to the formation of LSFL [14]. The Sipe-Drude model attributes HSFL formation to the second harmonic generation of the laser, which additionally acts on the interference at the irradiated surface [15].

After the first observation in 1965 [16] LIPSS have been widely created using different types of lasers and are most commonly created using femtosecond lasers. There have also been some studies on the creation of LIPSS using picosecond lasers. LIPSS have been observed in picosecond laser studies as early as in 1982 [17] when surface ripples were observed on silicon and gallium under picosecond laser illumination. Picosecond lasers have since been used to create LIPSS on several materials including semiconductors [18,19], metals [20], polymers etc. Eichstädta et al. [21] conducted a study on the formation of LIPSS using picosecond lasers, which outlines the theory to determine the parameters required to create uniform LIPSS over a large area. The study took into account the overlap between subsequent pulses and the accumulated fluence received at the surface. This study and other studies on creating picosecond LIPSS [22,23], however, use high overlapping ratios which limit the maximum scan speed. The effect of using low overlapping ratios and the resulting benefit of achieving high processing speeds has not been studied in the past for creating LIPSS using picosecond lasers.

Although reports of LIPSS created using femtosecond lasers are more prevalent in literature, there are several advantages picosecond lasers pose over femtosecond lasers for the application of creating LIPSS especially on semiconductors such as silicon. One of the primary benefits of using ultra short laser pulses lies in the fact that when the time duration of the pulse is shorter than the heat diffusion time, unwanted thermal damage of the material is prevented. The use of femtosecond lasers in processing metals is advantageous as the thermal diffusion time is close to 1 picosecond. However, since this diffusion time is higher in the case of semiconductors, often in the range of 10 ps - 100 ps

[24], there is no necessity to use expensive femtosecond lasers to process these materials. In addition to this, higher pulse energy and repetition rates can be achieved at a lower cost with picosecond lasers. Picosecond lasers are also more robust and are less sensitive, than femtosecond lasers, to fluctuations in operating conditions such as temperature and humidity. The high repetition rates of picosecond laser allow for faster processing speeds. These factors make it more cost effective and practical to use picosecond lasers instead of expensive femtosecond lasers for most material processing. These inherent advantages of picosecond lasers in the creation of LIPSS make it necessary to explore the full benefits in terms of process parameters. There is at present a lack of comprehensive knowledge on the effects of fluence, scanning speed, polarization and overlapping ratio on LIPSS created using picosecond lasers.

LIPSS have potential uses in several engineering applications such as creating hydrophobic surfaces and reducing fluid drag. Further, the tribological properties of materials such as friction and wear can be improved using LIPSS as has been demonstrated in studies using femtosecond lasers [9,25]. LIPSS due to their grating like structure can interact with incident light and alter the optical properties of the parent material. This can have several applications including light trapping for solar cell applications. There have been a number of studies on the light trapping properties of LIPSS, most of which have been using femtosecond lasers. Since high processing speeds at relatively lower costs can be achieved in creating LIPSS using picosecond lasers, it is required to study the properties of LIPSS created using picosecond lasers. The light trapping properties of LIPSS can be used to reduce surface reflections and thus reduce unwanted glare caused due to these reflections. The period of the LIPSS, which is

determined by the wavelength of the laser used and the accumulated fluence, can be varied to trap light over different wavelength ranges to create anti-reflective surfaces. This eliminates the need for ARCs which are expensive and susceptible to wear and damage. Since the period of LIPSS can be varied, certain wavelength ranges can be selectively absorbed resulting in a change in the color of the surface as has been demonstrated in some studies [26-28]. The light trapping properties of LIPSS will be discussed in detail in subsequent sections.

1.2.3   Hydrophobic surfaces

Surface wettability is commonly measured in terms of contact angle. Contact angle is the angle measured through the liquid, where a liquid–vapor interface meets a solid surface. Surfaces exhibiting a water contact angle below 90° are termed as hydrophilic surfaces while those with a water contact angle greater than 90° are termed as hydrophobic surfaces. Superhydrophobic surfaces have contact angles above 150°. Surface energy and roughness are the major contributing factors that determine whether a surface is wetting or non-wetting. The Cassie Baxter [29] and Wenzel [30] models are well-known empirical models that illustrate the nature of contact at the solid liquid interface. These models help predict the contact angle between surfaces and liquids. Another important parameter used to characterize the wetting nature of surfaces is the contact angle hysteresis. This can be measured as the difference between the advancing and receding contact angles at the instant before a droplet rolls off the surface as it is tilted. This is often used to characterize whether the surface is sticky or slippery. A small

contact angle hysteresis is desirable when slippery surfaces with low roll off angles are required.

Surface chemistry plays an important role in determining the wettability of a surface. The presence of high surface energy chemical groups such as –OH, -NH$_2$, -COOH, -OSO$_3$H, -NH$_3^+$, -COO$^-$, -OSO$_3^-$, promotes hydrophilicity, whereas materials such as hydrocarbon, fluorocarbon or silicone based polymers have low surface energy and exhibit hydrophobicity. Table 1.1. shows the surface energy and water contact angle of some common materials.

Table 1.1. Surface energy and water contact angle of some common materials.

Material	Surface Energy (dynes/cm²)	Contact Angle (degrees)
Clean glass	73	0
Ordinary glass	70	20
Polyester (PE)	47	70
Polycarbonate (PC)	46	75
Polyethylene terephthalate (PET)	42	76
Polymethylmethacrylate (PMMA)	41	82
Polypropylene (PP)	30	88
Polydimethyl siloxane (PDMS)	23	98
Paraffin	19	110

The two main forces acting to determine the shape of a liquid droplet are gravitational and surface tension forces. As the size of the liquid drop reduces the dominating force shifts from gravitational to surface tension. For water drops smaller than approximately 0.273 mm (one order of magnitude smaller than the capillary length of water = 2.73 mm) surface tension dominates. In addition to liquid-vapor surface tension (γ_{LV}), interfacial tension exists for the solid-liquid (γ_{SL}) and solid-vapor (γ_{SV}) interfaces as well [31]. When a droplet remains on a surface in a partial wetting state, there is an equilibrium contact angle θ_e, at the edge of the droplet. This is the tangent angle of the liquid-vapor interface at the three-phase (solid–liquid–vapor) contact line. The contact angle does not depend on the droplet size and is described by the Young equation given by Equation (1.2).

$$Cos\theta_e = \frac{\gamma_{SV} - \gamma_{SL}}{\gamma_{LV}} \qquad (1.2)$$

If $\gamma_{SV} < \gamma_{SL}$, the contact angle will be less than 90° and the surface is considered hydrophilic, whereas, if $\gamma_{SV} > \gamma_{SL}$, the contact angle will be greater than 90° and the surface is described as hydrophobic. There are two more possible cases of water resting on a surface. In the first case, the water is in complete contact with the entire surface which results in an increased surface contact. This is known as the Wenzel case. In this case the contact angle θ_w is given by Equation (1.3) [32].

$$Cos\theta_w = rCos\theta_e \qquad (1.3)$$

Where *r* is the factor by which the surface area is increased due to surface roughness as compared to the flat surface. The effect of hydrophobicity/hydrophilicity is essentially amplified by a factor of *r* in the Wenzel case. The second case is the Cassie Baxter case in which the liquid droplet rest on the surface features without maintaining complete contact with the surface. The liquid bridges the gaps between surface features in the solid. In this case, the contact angle θ_{CB} is given by Equation (1.4) [33].

$$Cos\theta_{CB} = f_s Cos\theta_e - (1 - f_s) \tag{1.4}$$

Where f_s is the fraction of the liquid contacted by the surface and the remainder $(1 - f_s)$ is the fraction of the surface area between surface features. Figure 1-2. demonstrates the 3 cases discussed.
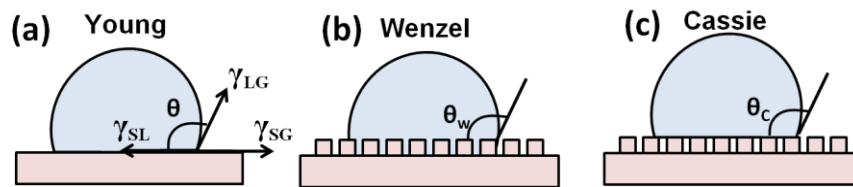
Figure 1-2. The different cases of liquid-solid interphase contact.

Therefore, surface roughness or structure is an important factor that determines the wettability of a surface. In general, the Wenzel state enhances the inherent wetting properties of surfaces, whereas, the Cassie Baxter state promotes hydrophobicity, thus leading to an increase in contact angle [34]. In many practical cases, an intermediate state between the Wenzel and Cassie Baxter modes is observed. The Wenzel state is usually observed in cases when water condenses onto the surface filling the gaps between

structures. The Cassie Baxter case is usually found when liquid drops are added to the surface.

There are several applications of hydrophobic and superhydrophobic surfaces in fields such as cell biological research, opto-fluidics, fuel cell research, drag reduction, printing, etc. The choice of materials, fabrication technique and degree of hydrophobicity required depends on the specific application. Microfluidics is one such field where surface wettability plays an important role. The contact angle and roll off angle of a liquid flowing through a micro channel influence the flow characteristics. Microfluidics are used in many applications such as DNA analysis, enzymatic analysis, clinical pathology among others, some of which require the flow rate in micro channels to be controllable. External flow control devices such as pressure generators and pumps are often used to control the flow rate through these devices. However, in cases where individual channels in a device are to be controlled, internal flow controls are required. This is often achieved by varying the channel cross section or by using flow control valves. A more space efficient alternative to this is to alter the wettability of channel walls so as to vary the flow rate through the channel. Chemical treatment of the channel inner walls is often done to achieve the desired contact angle. There are, however, disadvantages of using chemical methods to achieve hydrophobic channel walls. The cost of procuring, handling, storing and disposing chemicals adds to the fabrication cost. The presence of certain chemicals can interfere with and prohibit the use of some fluids in these devices. In addition to this, chemicals coatings can get washed away or deteriorate with time. There is currently the lack of quick and inexpensive techniques to accurately control the feature size and contact angle of features inside microfluidic channels.

The most commonly used material in microfluidics include polydimethylsiloxane (PDMS), silicon, glass, poly(methylmethacrylate) (PMMA), polycarbonate (PC), polystyrene (PS), polyethylene terephthalate (PET), polyvinyl chloride (PVC), hydrogels, paper and other composite materials. Of these, PDMS is the most popular for most applications as it has several advantages. It is a low cost and easy to micro fabricate material. It can be cast with nanometer resolution and is cheaper than glass and silicon. Since it has a low surface tension, it is easy to peel off from templates after curing. It is also easy to seal and bond to various surfaces including glass, silicon, PDMS etc. Since it is gas permeable it is compatible for cell culture [35]. Given these inherent advantages and the fact that PDMS has a contact angle greater than 90°, making it mildly hydrophobic, it is a good choice for microfluidic applications.

1.3   Literature Review

1.3.1   Surface texturing for solar cell applications

Texturing the surface of silicon wafers to suppress reflections has been commonly used to improve the efficiency of solar cells. Surface texturing for solar cell applications dates back to the late 1960s. In the 1970s, Gittleman et al. [36] created pillars on the surface of silicon using reactive sputter etching. Following this several studies were conducted on the fabrication [37,38] and modeling [39] of anti-reflective surface structures. The light trapping effect of surface structures on solar cell surfaces is attributed to multiple surface reflection which improves the probability of incident light being absorbed by the surface. In addition to this, some surface nano structures result in a

gradient refractive index, which decreases interfacial reflections by creating a continuous refractive index gradient between the bulk of the material and the surrounding medium as seen in Figure 1-3. ARCs on the other hand rely on destructive interference of reflected light and require the careful selection of coating materials and thickness. The AR effect of single layer ARCs is not broadband and the addition of multiple ARC layers increases production cost.
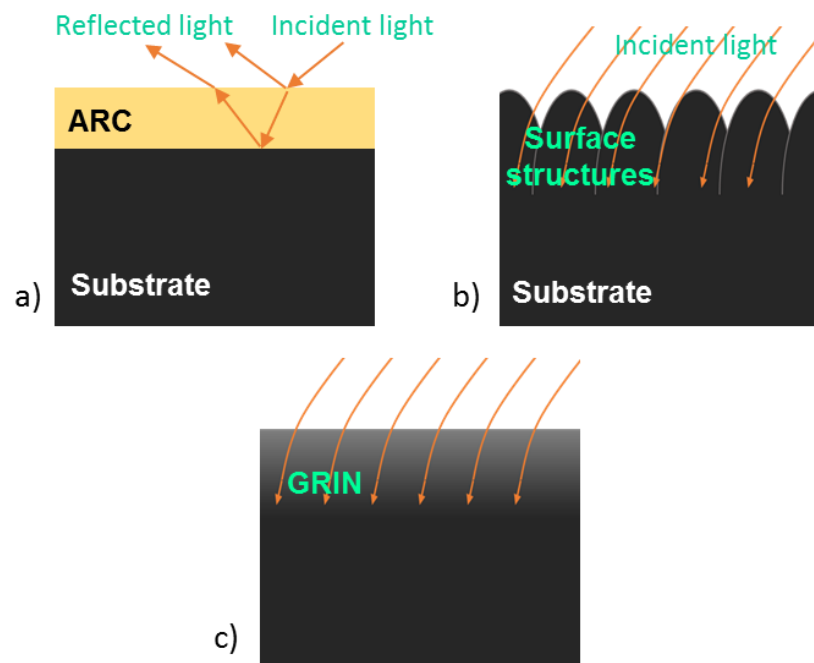
Figure 1-3. a) Propagation of light through single layer ARC, b) Gradient refractive index due to subwavelength-size nanostructures, c) Schematic of the refractive index change due to nanostructures in b).

The efficiency of a solar cell is calculated as the ratio of the maximum power output to the product of the incident radiation flux and the collection area. Reducing the surface reflectance increases the power output or makes the solar cell more compact. Since less of the incident light is lost to surface reflection, the cell is provided with more

photons for energy conversion. This increases the current density and as a result the power output increases. Thus a decrease in the surface reflectance of solar cells results in an increase in the overall efficiency of solar cells. The contributions to loss of efficiency from other factors such as recombination and thermalization remain constant and thus the overall efficiency improvement can be estimated based on the change in reflectance. A direct correlation between the two has been shown in several studies. Chen et al. [40] fabricated a nano patterned PMMA layer using e-beam lithography and chemical wet etching, which was used as an ARC on a silicon solar cell. The coating suppressed the surface reflectance in the range of 200 nm and 1000 nm to under 15%, resulting in the improvement of overall efficiency from 10.4% to 13.5%. Similarly, Song et al. [41] created submicron gratings on thin film crystalline silicon solar cells using interference lithography to reduce the surface reflectance in the wavelength range of 300 nm and 1200 nm to less than 10%. This resulted in the improvement of overall solar cell efficiency from 8% to 14% for normal incidence of light. Alkaisi et al. [42] fabricated nanopyramid structures in crystalline silicon solar cells, which reduced the surface reflectance over the visible spectrum to under 10%. This resulted in an improvement in overall efficiency from 4.03% to 6.73%. The change in surface reflectance and the corresponding increase in efficiency in these and several other studies [43-46] reveals a nearly linear trend of increasing efficiency with decreasing reflectance. Therefore, a good estimate of efficiency improvement can be made based on absorptance improvement.

Several different surface structures have been shown to greatly suppress surface reflections in solar cells. Sun et al. [47] created bio inspired broadband anti-reflective moth eye structures on single crystal silicon by templating, resulting in less than 2.5%

reflectance over the wavelength range of 350 nm to 850 nm. Zhu et al. [48] created nanodome structures on silicon through a multilayer deposition process to achieve 94% absorption over the wavelength range of 400 nm to 800 nm. Mavrokefalos el al. [49] fabricated inverted pyramids in crystalline silicon using wet etching. Wang et al. [50] analyzed the light trapping by nano cone structures in ultrathin silicon solar cells and recommended the fabrication via reactive ion etching while Hu et al. analyzed the optical absorption in silicon nanowire arrays [51]. Cao et al. [52] created pyramid and nanowire binary structures on silicon through a multi-step chemical etching process and achieved a 0.9% reflectance over the wavelength range of 200 nm to 1000 nm. Despite the low reflectance values achieved, most of the methods discussed above are expensive, time intensive or require complex fabrication procedures.

Laser surface texturing has also been widely used as a one-step process to suppress surface reflections in solar cell applications. Dobrzański et al. [53] textured multi crystalline silicon solar cells using an Nd:YAG laser creating various micro groove and grid patterns. Sedao et al. [54] used a femtosecond laser to create micro cones on silicon achieving under 7% reflectance over the wavelength range of 400 nm to 1200 nm. Vorobyev et al. [55] used direct femtosecond laser irradiation to create black silicon in the form of microgrooves textured with nanostructures. The reflectance of the surface was below 5% across the visible spectrum.

Grating structures are also known to exhibit anti-reflective properties. Gaylord et al. [56,57] used a rigorous coupled-wave analysis to study the anti-reflective effect of high spatial frequency rectangular groove dielectric gratings. They reported that zero reflectivity can be achieved through grating structures and studied the dependence of

reflectivity on filling factor (defined as the percentage of the grating period consisting of solid), groove depth, angle of incidence, and polarization. Ono et al. [58] modeled the anti-reflective effect in holographic relief gratings based on the gradient refractive index effect. They showed that sinusoidal gratings are anti-reflective over broad wavelength ranges at almost any depth. Raguin et al. [59] theoretically studied the anti-reflective effect of one dimensional surface gratings. These and other studies [60] laid the foundation for grating-based anti-reflective surfaces for solar cell applications. The wavelength range over which the surface reflections are suppressed is influenced by the geometry of the grating [61]. These structures are commonly used to create ARCs by methods such as mechanical scribing, lithography, etching, spin coating replication, vapor deposition, etc. [62-64].

There have been studies to determine the optimal period and height of periodic surface ripples to maximize light trapping in solar cells. Čampa et al. [65] conducted a study on silicon solar cells with periodic sinusoidal textured interfaces in order to optimize the spacing period (p) and the height (h) above the surface of periodic structures on the surface of silicon solar cells. A model was created using finite element method (FEM) to simulate structures that minimize total reflectance. The results showed a number of period and height combinations that suppress reflectivity in the wavelength range of 350 nm to 1000 nm. The optimum structure determined was a period of 700 nm and a corresponding feature height of 450 nm. The simulation predicted that this structure would increase the short circuit current density in a solar cell by 45% compared to a cell with a flat un-textured surface. Other configurations such as 600 nm in period with 150 nm in height and 550 nm in period with 300 nm in height also result in large

improvements of 40% in short circuit current density. The simulations reveal that with

taller surface features, a further increase in short circuit current can be achieved. It can be

concluded that higher structures are favorable and must be generated to achieve higher

absorptance; however, it is challenging to create structures with high aspect ratios (h/P).

Devan et al. [66] investigated the optics of microcrystalline silicon thin-film solar

cells with integrated light trapping periodic structures. The quantum efficiency and the

short circuit current density were measured for different configurations of periodicities

ranging from 300 nm to 500 nm and grating heights varying from 0 to 500 nm. The

investigation was done by the numerical simulation of Maxwell's equations utilizing the

finite difference time domain (FDTD) algorithm. The wavelength range of incident light

used in the study was 300 nm to 1000 nm corresponding to the bandgap of silicon. It was

found that the optimal grating period is 600 nm and the optimal groove height is 300 nm.

Solntsev et al. [67] studied the effect of submicron periodic gratings on light absorptivity

in thin film silicon solar cells over the wavelength range of 0.66 µm to 1 µm. The

photocurrent generated was simulated using FDTD simulations for a variety of

periodicities and heights and compared to the photocurrent of a flat surface, from which

the best combination of grating periodicity and height was determined. It was found that

the maximum light absorptivity enhancement was observed for a grating periodicity of

500 nm and a grating height of 550 nm. Several other studies on the effect of surface

grating on the light absorptivity of solar cells have been conducted and the results are all

similar to those of the studies discussed above. A study by Haase et al. [68] reported that

the short current is maximized if the grating period is equal to 700 nm and the groove

height is equal to 330 nm over the wavelength range of 700 to 1100 nm. A 50% fill factor

was assumed in this study. Another study by Catchpole [69] analyzed the coupling of light into a solar cell. They concluded that the optimal grating period is 650 nm and the optimal groove height is 300 nm to 350 nm for a ZnO/silicon grating structure. Yet another study by Ganapati et al. [70], which used electromagnetic optimization to design light trapping textures on subwavelength thickness solar cells , concluded that the optimal period is 710 nm.

From the studies above, it can be concluded that the optimal period and structure height to suppress surface reflectivity and improve light absorptivity within the wavelength range best suited for solar cell applications are approximately 600 nm and 300 nm respectively. One method to create grating like surface structures is through the formation of laser induced periodic surface structures (LIPSS).

Vorobyev et al. [71] first studied the anti-reflective effect of LIPSS created on the surface of silicon in 2011. Using a femtosecond laser, uniform LIPSS were created with a period of 575 nm. The scan speed used in this study was only 1 mm/s and a high overlapping ratio between pulses was used. The resultant surface had a reflectance in the range of 10% to 30% over the wavelength range of 250 nm to 2500 nm. Ionin et al. [72] created femtosecond LIPSS on the surface of GaAs while maintaining a high pulse overlapping ratio and a scan speed of 375 µm/s using a cylindrical lens. A 744 nm wavelength laser was used to create LIPSS with a period of 650 nm. The study reported a 42% decrease in surface reflectance at a wavelength of 2500 nm. More recently, Dar et al. [73] reported femtosecond LIPSS on titanium with broadband low reflectance. A scan speed of 0.2 mm/s was used to achieve 650 nm period LIPSS, which reduced the reflectance over the range of 800 nm to 2000 nm from approximately 46% to less than

1%. These studied however, were limited to high overlapping ratios and low processing speeds.

1.3.2   Surface texturing for superhydrophobic surfaces

The wettability of solid surfaces has been a subject of interest for many years due to the wide ranging applications involving such interactions. The earliest reports on hydrophobicity of surfaces date back to the early 1900s [74] and several studies have been reported on contact angle and wettability of different materials over the last few decades [75-79]. More recently, with the advancements in nano technologies, several studies have been reported on creating and analyzing hydrophobic surfaces, many of which have taken inspiration from naturally occurring hydrophobic surfaces such as the lotus leaf [80-82]. Patankar et al. [83] proposed a dual scale surface structure mimicking the lotus leaf and theoretically calculated the optimal structure geometry to achieve self-cleaning superhydrophobic surfaces.

There have been many studies to understand the effects of surface structure on the wettability of materials. Nosonovsky et al. [84] identified a set of requirements for optimized roughness distribution for achieving high contact angles. The following guidelines were provided for designing hydrophobic surfaces:

1. Roughness should be hierarchical, with several scale sizes, from microbumps to nanobumps. Largest asperities should be small compared to maximum droplet size, given by the capillary length.

2. Asperities should be high with their height limited by the requirement of their structural strength. It is known that the strength of geometrically similar structures

increases with decreasing scale, since forces (e.g., weight) are usually

proportional to volume and therefore the third power of length, while strength is

proportional to the cross-section area and thus to the second power of length.

3. Asperities at each scale level should have small-width and large distance between

    them; however, this requirement is limited by some critical value of the spacing

    between asperities, providing the ability to support required pressure.

4. Nanoasperities should be convex (bumps rather than grooves) to stabilize the

    liquid–air interface.

5. For initially hydrophilic surface, a hydrophobic coating is required.

Marmur [85] analyzed different wettability states in terms of thermodynamic equilibrium and stability. The study proposed mathematical conditions that promote non-wetting and provided design principles for achieving non-wettability. Bormashenko [86] performed an extensive literature study highlighting the physical mechanisms of wetting transitions and the effect of surface roughness on such transitions.

Several methods to create hydrophobic surface have been reported in literature, which include both chemical treatments to reduce surface energy and surface structuring to increase surface roughness. The methods to create hydrophobic surface structures include lithography, chemical vapor deposition, sol-gel process, plasma etching, laser texturing, crystal growth, and several others [87-90]. Figure 1-4. shows some superhydrophobic surfaces structures reported in literature using various fabrication processes.
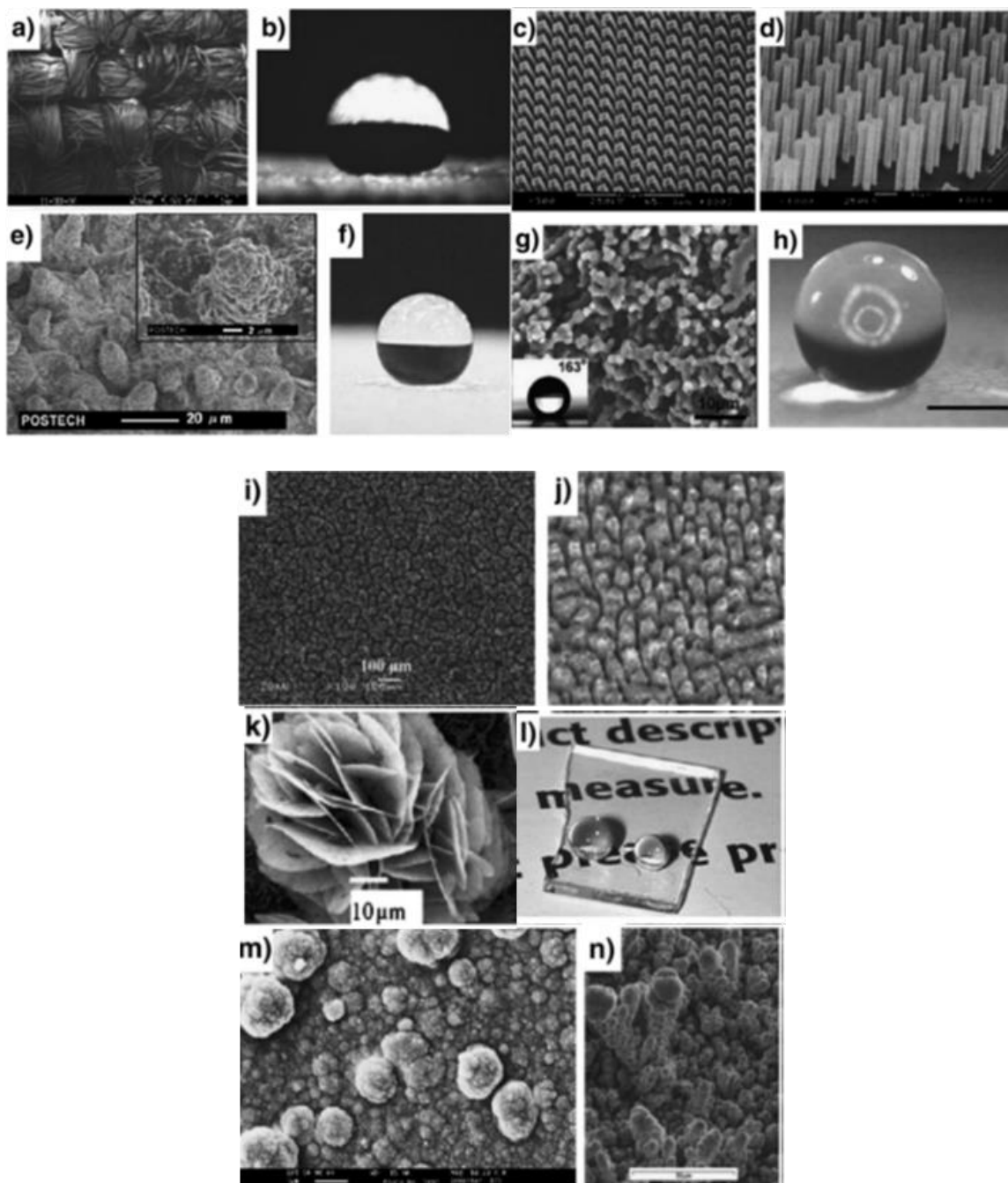
Figure 1-4. Superhydrophobic surfaces prepared in different ways, highlighting the various topographies possible a), b), textile superhydrophobic surfaces; c), d) Lithographic patterns; e), f) Templating; g) h), phase separation; i) j), Etching; k), l), crystal growth; m), n) diffusion limited growth.

Laser texturing has been used as a one step process to create surface structures on various materials to achieve varying degrees of hydrophobicity. Kietzig et al. [91] conducted a parametric study using femtosecond laser irradiation to create self-formed superhydrophobic micro and nano structures on various steels and titanium alloys. Rukosuyev et al. [92] created micro grid patterns on the surface of stainless steel by femtosecond laser ablation and showed that the superhydrophobicity achieved was due to structure and not intrinsic material properties. Vorobyev et al. [93] created surface structures on Titanium using femtosecond laser pulses to achieve hydrophobicity as well as anti-reflective properties. Duong et al. [94] studied the conversion of nanosecond laser textured copper and brass from hydrophilic to hydrophobic and attributed the change to the partial de-oxidation of CuO into Cu_2O. Baldacchini et al. [95] demonstrated laser treatment following chemical treatment such as silanization can be used to decrease the surface energy and achieve hydrophobicity. Following this, many studies utilized silanization of laser textured surfaces to achieve hydrophobicity. Wu et al. [96] created femtosecond LIPSS on stainless steel and silanized the surface to achieve superhydrophobicity. Jagdeesh et al. [97] used a picosecond laser to create dual scale micro nano structures on steel and titanium alloys followed by silanization to create superhydrophobic surfaces. Long et al. [98] also used a picosecond laser to create periodic nano structures on copper followed by silanization to achieve superhydrophbic and colorful surfaces. Over the last few years, several other researchers have used this technique to create superhydrophobic surfaces on different materials [99-101]. All these previous studies were done on metals and little work has been done in this area on polymer surfaces.

In the case of microfluidic channels, surface texturing to achieve superhydrophobicity is often done using chemical treatments. This is done using methods such as modification with octadecyltrichlorosilane (OTS) self-assembled monolayers (SAMs) [102], aerosol assisted chemical vapor deposition (AACVD) [103], plasma deposition of octafluorocyclobutane (C_4F_8) [104] and other methods [105]. Alternatively, attempts have been made to make the surface of the inner channel walls rough using methods such as plasma treatment [106]. Despite all these, there is currently the lack of quick and inexpensive techniques to accurately control the feature size and contact angle of features inside microfluidic channels.

1.4   Research Objectives

The primary objective of this research is to create desirable surface textures using ultra short pulse lasers to enhance material properties for engineering applications. The research is also focused on improving processing speeds and reducing cost to make processes adaptable to industrial requirements.

The specific goals of the research are as follows:

1) Improve solar cell overall efficiency through the design and fabrication of light trapping surface structures at high processing speeds. Optimize the geometry and enhance processing speed of LIPSS texturing to enhance light trapping in solar cells.

2) Determine the predictability of surface reflectance of laser textured surfaces through computer simulations.

3) Design and fabricate superhydrophobic surface structures on metals and polymers.

4) Enhance the fluid flow rate through microfluidic devices by incorporating superhydrophobic surface structures.

1.5 Overview of the Thesis

This chapter deals with the background information, literature review, research objective of the thesis. Chapter 2 describes the experimental details of texturing silicon using a picosecond laser to improve solar cell efficiency. The experimental results are compared with computer simulations to determine the predictability of surface reflectance of textures surfaces. The texturing of CIGS thin film solar cells is also discussed. In Chapter 3 the experimental details of creating and characterizing superhydrophobic surfaces is discussed in detail. The transfer of surface nano structures from metals to polymers is discussed. In addition to this, a process to fabricate microfluidic devices with controllable fluid flow rate is presented. Chapter 4 enlists the key conclusions and findings of this work and also provides recommendations for future work.

CHAPTER 2. LIPSS IN SOLAR CELL APPLICATIONS

As discussed in the previous chapter, periodic surface structures can be used to reduce the reflectivity of surfaces. The range of wavelengths for which reflectivity is suppressed depends on the geometry of the structures created. In order to determine the range of wavelength for which reflectivity must be reduced to improve solar cell efficiency, the intensity distribution of the solar spectrum was studied. Figure 2-1. shows that the majority of the solar energy received at the earth's surface is in the visible and near infrared wavelength range.
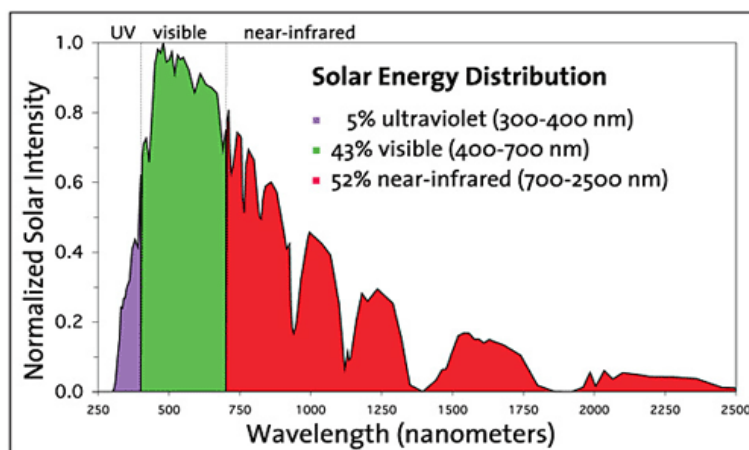
Figure 2-1. Solar irradiance spectrum [107].

By comparing the solar irradiance spectrum with the crystalline silicon photoelectric conversion spectrum it can be seen that within the bandgap range of silicon, the highest spectral irradiance at sea level for AM 1.5 G solar spectrum is between 400

nm and 900 nm. This can be seen in Figure 2-2. This is the ideal range for reflectance reduction to maximize silicon solar cell efficiency improvement.
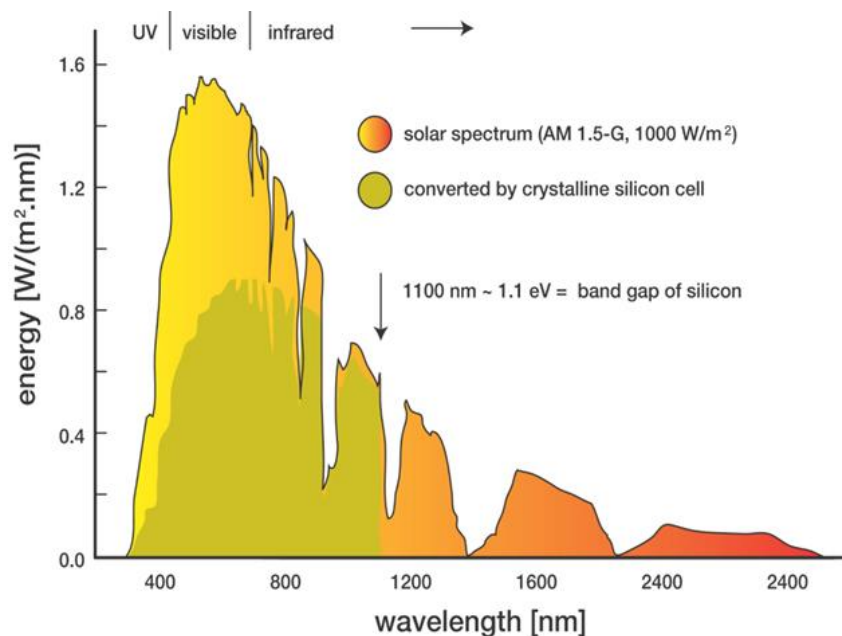
Figure 2-2. Solar spectrum and silicon solar cell optical bandgap [108].

The following sections describe the experimental details of creating light trapping surface nano structures to improve solar cell efficiency. The modelling of light trapping structures and FDTD simulations are discussed. The simulation results are compared with reflectance test results of the fabricated samples.

2.1   Experimental Details

2.1.1   Laser setup and imaging techniques

A Lumera Rapid Picosecond laser was used to create LIPSS on silicon wafers. The laser generates linearly polarized pulses with a pulse duration of 10 ps at 1064 nm

and 532 nm with a variable repetition rate ranging from 10 KHz to 640 KHz. A half wave

plate was used to rotate the angle of polarization. A beam expander was used to create a

collimated and expanded beam which was directed into a laser scanner head. The scanner

head contains high speed mirrors and an 80 mm focal length objective lens. The laser

beam focal spot size used was 10 µm. A computer controlled precision 3-axis stage was

used to position the silicon sample under the scanner head. The silicon samples used are

127 mm diameter, 525 µm thick polished wafers. The silicon is N doped with

phosphorous and its crystal orientation is (111) with the electrical resistivity less than

0.006 ohm-cm. In order to create LIPSS, the laser was scanned over the surface of the

wafer, which was positioned at the focal length of the objective lens. Long scans were

made in the x direction with small shifts in the y direction to create a large scanned area.

All experiments were conducted with ambient air as the irradiation atmosphere. Figure

2-3. shows a schematic of the laser setup used to create LIPSS.
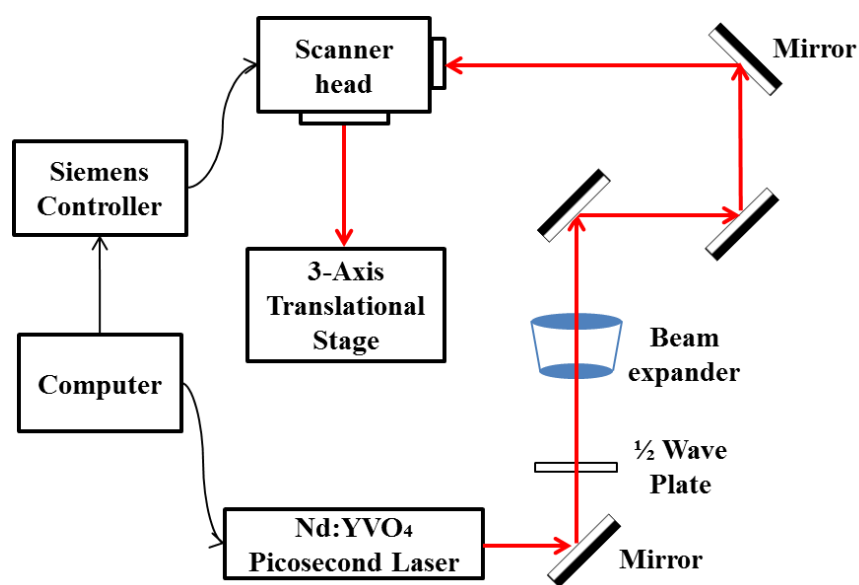
Figure 2-3. Picosecond laser setup used to create LIPSS.

To study the surface structures created on the sample, preliminary observations were made using an optical microscope, followed by SEM imaging. The samples were first cleaned in an ultrasonic cleaner with acetone, followed by methanol to dislodge loose particles and to free the sample from organic impurities that may have been present. Due to the low electrical conductivity of the sample, charging was expected during SEM imaging. To prevent charging, the silicon samples were sputter coated with platinum before imaging. AFM imaging was also done to study the profile of the structures formed. In order to study the composition and crystallinity of the silicon wafer before and after the creation of LIPSS on the surface, EDS and XRD analyses were performed.

2.1.2   Picosecond LIPSS on silicon

Initial experiments to determine the parameters needed to achieve large area uniform LIPSS on the silicon surface were conducted at a laser wavelength of 1064nm. At a fluence value of 0.8 J/cm^2, uniform LIPSS were created on a small area. SEM and AFM imaging was done to study the profile and geometry of the structures. Figure 2-4. shows an AFM image of the LIPSS created at 1064 nm wavelength. The average valley depth was measured to be 300 nm while the maximum valley depth was nearly 400 nm. As expected, the structures had a period of 1064 nm, which was the same as the wavelength of the laser used. Figure 2-5. shows an SEM image of LIPSS created using a 1064 nm wavelength laser.
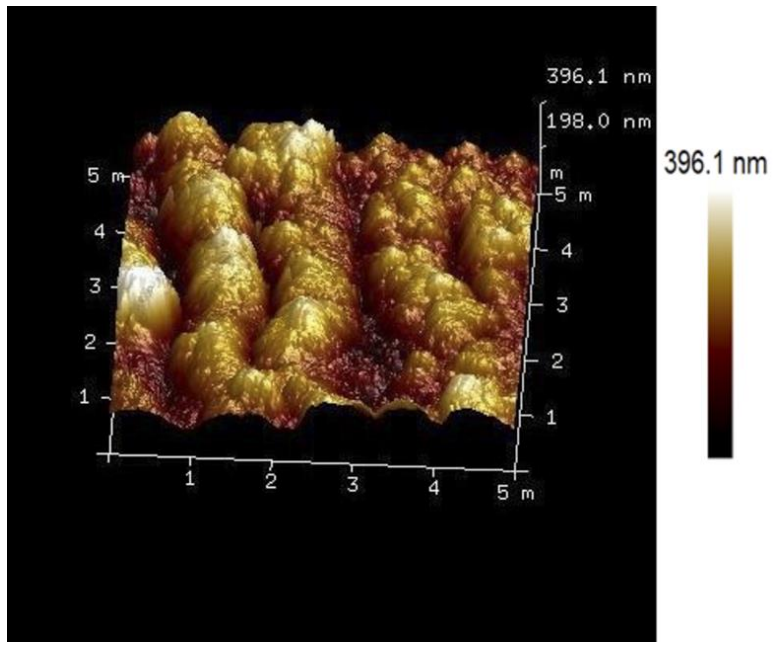
Figure 2-4. AFM image of LIPSS created using a 1064 nm wavelength laser showing maximum valley depth.
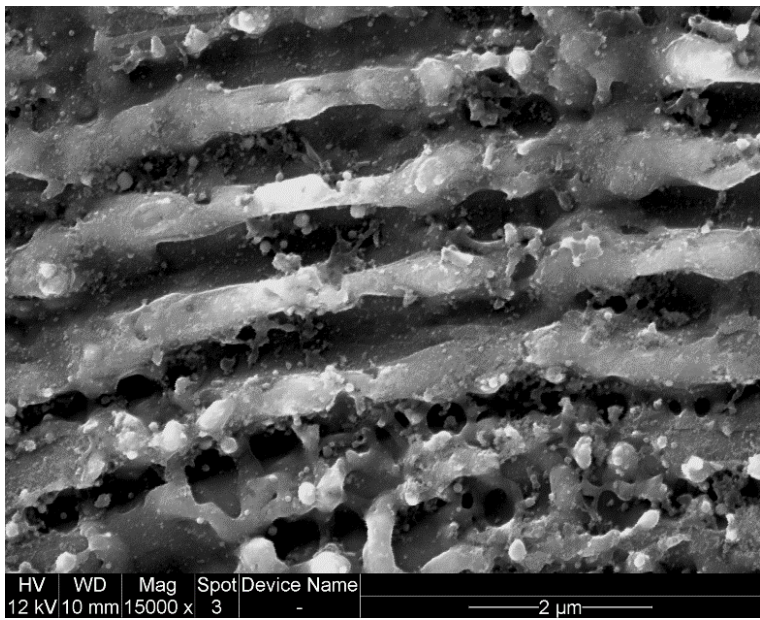
Figure 2-5. SEM image of LIPSS created using a 1064 nm wavelength laser.

In order to determine the period required to achieve the lowest surface reflectance, FDTD simulations were conducted. The simulation set up is described in

detail in section 2.2. The period of the grating structures was varied and the effect on reflectance was studied. When the period was varied from 1100 nm to 400 nm in steps, it was determined that a period close to 450 nm was the most effective in suppressing reflections in the wavelength range of 200 nm to 1100 nm. This is the range of wavelengths in which silicon solar cells convert light energy to electrical energy. Since LSFL have a period nearly equal to the wavelength of incident laser radiation, the 532 nm wavelength of the picosecond laser was chosen. The focus in this study was to suppress reflections in the range of 400 nm to 860 nm, which is a range of high solar intensity for silicon solar cells. The 532 nm laser pulses were scanned over the silicon wafer at a repetition rate of 10 KHz. The scan speed was increased to gradually reduce the overlapping ratio from 99.9% to 50%. The power was simultaneously increased to maintain the fluence required to form LIPSS. It was observed that uniform LIPSS could be generated for overlapping ratios ranging from 99.9% down to 60%. Below 60%, gaps appeared between adjacent pulses and the LIPSS became discontinuous. In order to maximize processing speed, an overlapping ratio of 60% was chosen and a scan speed of 60 mm/s was maintained. Uniform LIPSS over a large area were created through parallel line scans with small shifts normal to the scanning direction, while maintaining the overlapping ratio.

To study the effects of changing the laser beam polarization angle, a half wave plate was used in the beam path. The wave plate was rotated to change the angle of polarization and the resultant LIPSS were studied. Varying the angle of polarization resulted in a change in the orientation of LIPSS without a change in the LIPSS period or profile. As the polarization angle was rotated from being normal to the scanning direction

to being parallel to the scanning direction, the LIPSS rotated by 90°. When the LIPSS were no longer parallel to the scan direction, it became necessary for the pulses in the adjacent parallel scan lines to be aligned such that continuous LIPSS could be formed normal to the new polarization direction. This was achieved through small changes in the scan length to ensure a perfect overlap between pulses in adjacent scan lines. For the remaining experiments, the polarization direction was chosen normal to the scanning direction so that LIPSS were parallel to the scanning direction. EDS and XRD analyses revealed no change in composition and crystallinity of the sample before and after the creation of LIPSS.

It was observed that below the fluence of 0.7 J/cm^2, no damage was visible on the surface of silicon. Above this fluence, LIPSS were formed and the structures were more prominent with deeper valleys as the fluence was further increased. In order to maximize the processing speed, the repetition rate was gradually increased from 10 KHz to 640 KHz in steps. At each step the power and the laser beam scan speed were increased to maintain the overlapping ratio and fluence required for the formation of LIPSS. It was observed that as long as the fluence was maintained, the scan speed had no impact on the structures formed. At 640 KHz a scan speed of 4000 mm/s was used to create uniform LIPSS over an area of 4 cm by 4 cm.

SEM images revealed that the LIPSS had a period of 532 nm and a fill factor of 75%. The depth of the channels was found to increase with increasing fluence. At 0.7 J/cm^2, ripples were faintly visible with minimal variation in height between crests and troughs. At 0.8 J/cm^2 highly uniform structures were obtained with no surface material removal. The periodic structures appeared to have flat top surface with filleted edges and

deep narrow valleys. The depth of the valleys was determined through AFM imaging and found to range from 150 nm to 350 nm. Figure 2-6. shows SEM images of the highly periodic LIPSS created at a fluence of 0.8 J/cm^2. Figure 2-7. shows the progressive changes on the formed nanostructures with increasing laser fluence. At 1 J/cm^2 some material removal was observed and the deeper valleys were formed Figure 2-7. b. The structures were still periodic and the ripples were continuous with minor breakages. At 1.2 J/cm^2 the material removal caused breakage of the LIPSS and the structures were not continuous Figure 2-7. d. The surface also appeared dull grey possibly due to mild oxidation on the surface and lower surface reflectance. The valleys however appeared deeper and smaller nanostructures were present on the surface. These nanostructures may have resulted from the sputtering of the parent silicon onto surrounding areas.
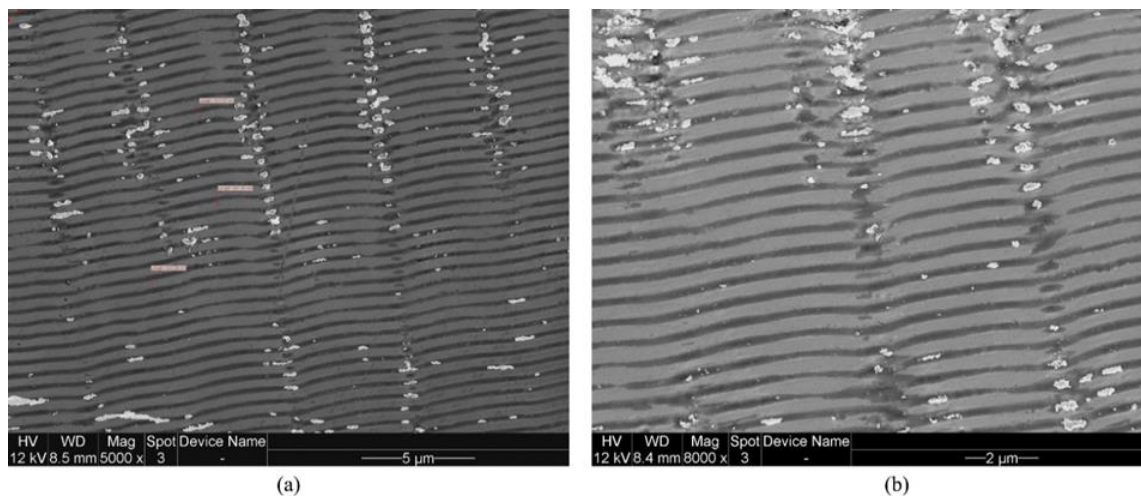
Figure 2-6. SEM images of highly uniform LIPSS created at a fluence of 0.8 J/cm^2. a) at 5000x magnification b) at 8000x magnification.
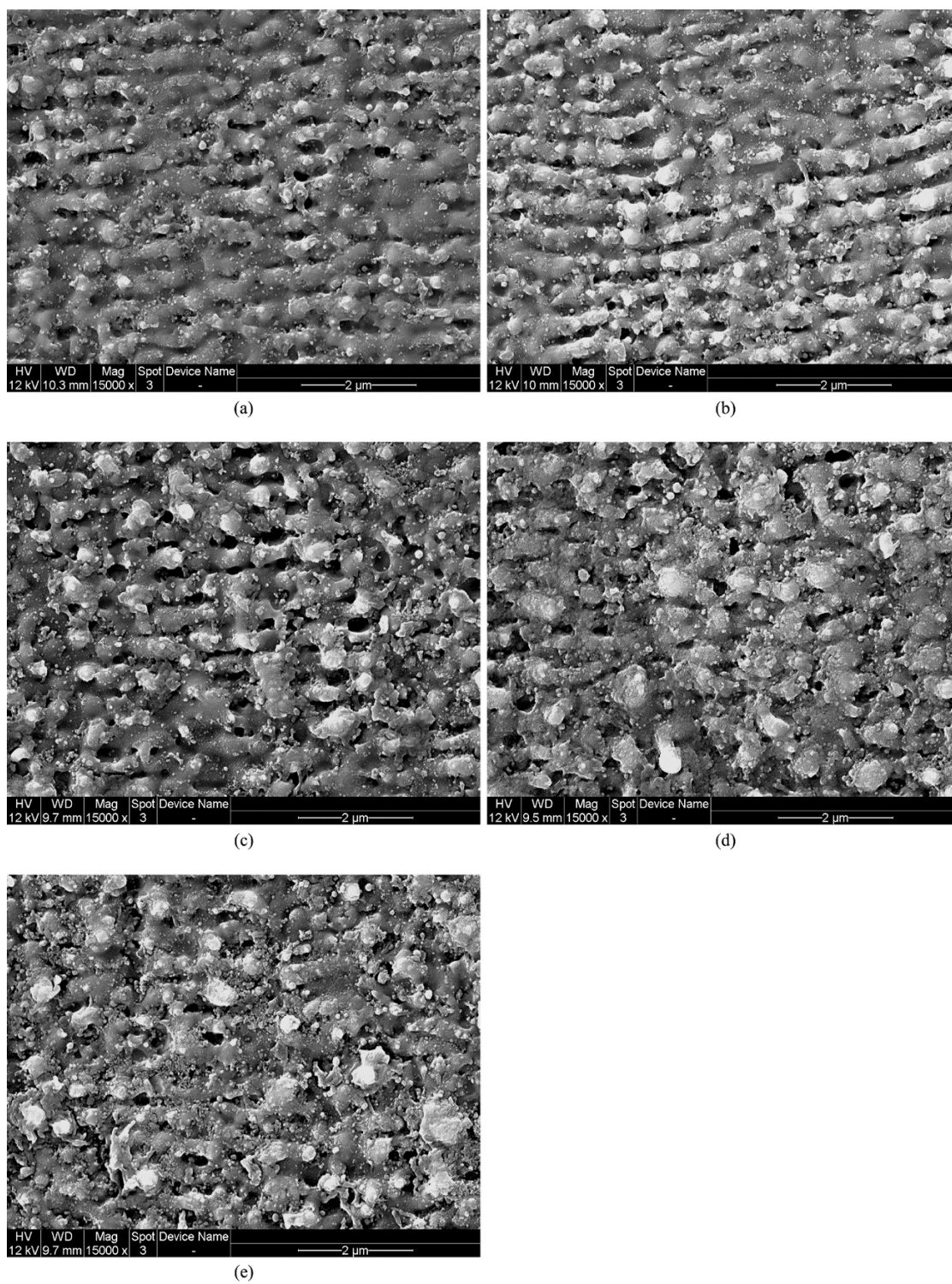
Figure 2-7. SEM image of nanostructures created at a fluence of a) 0.95 J/cm^2 b) 1 J/cm^2 c) 1.1 J/cm^2 d) 1.2 J/cm^2 e) 1.3 J/cm^2.

Visual observation of the textured silicon wafer revealed iridescence when viewed under a broadband light source as shown in Figure 2-8. Different viewing angles measured from the horizontal, resulted in different colors. This is attributed to structural coloration as a result of interference effects caused by the grating like LIPSS. At 0° the sample appeared grey as seen in Figure 2-8. a. As the angle was increased from 3.5° to 11.5° in steps of 2° various colors were observed. This iridescent effect was seen only in structures created at fluence values between 0.7 J/cm^2 and 1 J/cm^2. Above this fluence value the surfaces began to appear dull and grey possibly due to increased light trapping.
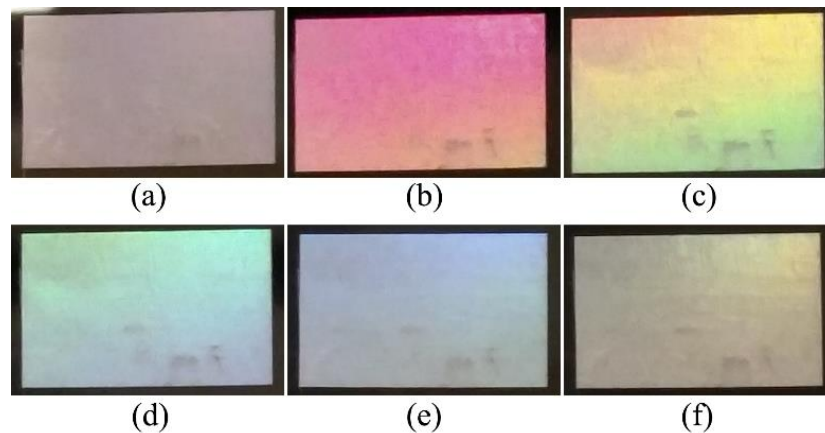
Figure 2-8. Photographs showing iridescent effect of area covered with LIPSS when viewed at different angles to the horizontal: a) 0° b) 3.5° c) 5.5° d) 7.5° e) 9.5° f) 11.5°.

2.1.3   Reflectance tests

In order to measure the broadband reflectance of the sample, a Perklin Elmer Lambda 950 spectrophotometer with an integrating sphere accessory was used. First the sample was checked for opacity and then the spectral reflectance (R) and transmittance (T) were measured over the wavelength range of 200 nm to 1200 nm. A monochromator

was used to resolve the wavelength. A blank wafer with no texturing was used to calibrate the machine and its reflectance values were used for comparison with textured samples. Reflectance tests were conducted on the samples to study the effect of LIPSS on surface reflectance. Structures created at the same fluence value exhibited the same reflectance across the wavelength range of 200 nm to 1100 nm, irrespective of the scan speed and repetition rate used. Structures created with the same fluence appeared identical under the SEM and thus were expected to exhibit the same reflectance. Structures made with increasing fluence values exhibited a trend of decreasing average reflectance value. As the fluence was increased from 0.95 J/cm^2 to 1.4 J/cm^2, the average reflectance over the wavelength range of 400 nm to 860 nm decreased from 25.79% to 19.84%. As compared to the reflectance of bare silicon which was measured to be 35.93% over the same wavelength range, a 44.8% decrease in reflectance was achieved for the case of texturing at 1.4 J/cm^2. This drop is attributed to the increasing depth of channels and increasing irregularities on the surface.

At fluence values close to 0.8 J/cm^2, highly periodic and continuous LIPSS are formed with shallow valleys which are not very effective in trapping incident light. At higher fluence values up to 1 J/cm^2 the valley depth was found to increase and light was trapped more effectively. At a fluence of 1.1 J/cm^2, deep and continuous LIPSS were formed resulting in an average reflectance of 23.1% corresponding to a 35.7% decrease in average reflectance compared to bare silicon. At even higher fluence values up to 1.2 J/cm^2, deep valleys were created with irregularities due to material removal. This resulted in even lower reflectance values due to increased scattering of light below the surface of the material. Beyond this fluence value, the structures no longer appeared periodic. Deep

craters and surface irregularities were formed which further enhanced scattering and light trapping below the surface, thus decreasing the average reflectance. Figure 2-9. shows the reflectance curves for structures created at different fluence values, across the wavelength range of 400 nm to 860 nm. A clear decreasing trend in reflectance is seen as the fluence is increased. Above this fluence, material removal causes severe damage to the surface.
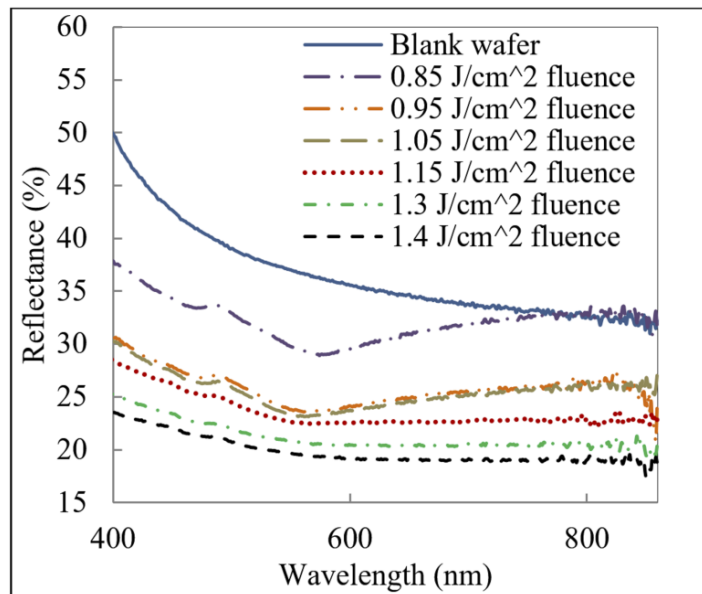
Figure 2-9. Reflectance curves showing a decreasing trend in reflectance with increasing fluence values.

The results indicate that random nanostructures are more effective in reducing surface reflection than periodic structures. As the fluence was increased and the structures transitioned from being highly periodic to random structures, there was a drop in average reflectance as well. This is in agreement with a study on disordered arrays of silicon nano-wires by Bao et al. [109], which also reported lower reflectance values with random surface structuring when compared with periodic uniform structures. To study the effects of a thin oxide layer on the textured surface, simulations were run and are

discussed in section 3.3. The results show that the effect of a thin oxide layer, if present, is negligible. Prior to reflectance testing, the samples were chemically cleaned in an ultrasonic bath. This ensures all organic impurities and surface particles which are loosely held are removed and do not influence the surface reflectance.

2.2 Finite Difference Time Domain Simulations

In order to validate the experimental results and to study the predictability of the reflectance values of LIPSS, computer simulations were conducted. In addition to this, simulations were conducted with different periodic geometries to study the effect of changing profiles on the reflectance. The commercial software Lumerical FDTD was used in this study. The software solves Maxwell's curl equations in non-magnetic materials. The governing equations are given by Equations (2.1) to (2.3).

$$\frac{\partial \vec{D}}{\partial t} = \nabla \times \vec{H} \tag{2.1}$$

$$\vec{D}(\omega) = \varepsilon_0 \varepsilon_r(\omega) \vec{E}(\omega) \tag{2.2}$$

$$\frac{\partial \vec{H}}{\partial t} = -\frac{1}{\mu_0} \nabla \times \vec{E} \tag{2.3}$$

where H, E, and D are the magnetic, electric, and displacement fields, respectively, while ε_r is the complex relative dielectric constant.

Simulations were performed to calculate the reflectance value over a unit cell of the structured silicon wafer. To validate the experimental results, the profile of the unit

cell was modeled based on the AFM and SEM images of the structures formed in experiments. Since the structures were highly periodic, a single unit cell was sufficient to fully represent the surface structure. Also, a 2D simulation was sufficient to represent the structure as the grating cross section remained constant in the third dimension. The mesh size was set using the conformal mesh technology, which determines the required non uniform mesh size to ensure convergence. A high accuracy mesh setting was used, which provides a typical mesh size of 26 to 30 points per wavelength. The time step is automatically calculated from the simulation mesh size based on the Courant stability criterion. A periodic boundary condition was used along the x axis (parallel to the silicon surface) to simulate a repetitive structure. For the y- axis, (normal to the surface) perfectly matched layer (PML) boundary condition was used to absorb unwanted reflections and prevent them from re-entering the simulation domain. A plane wave source was used to normally inject electromagnetic energy on the surface. The resultant reflectance spectrum was multiplied with the AM 1.5G solar spectrum to simulate sunlight incident on the surface. Comparative studies between experiments and simulations were done for the periodic structures formed at a fluence value of 0.85 J/cm^2. The fill factor, defined as the percentage of the grating period consisting of silicon, was measured to be 75% and the depth was 350 nm. The top surfaces of the ripples appeared flat and the edges were rounded.

A good match between experimental and simulated values of reflectance was obtained as can be seen from Figure 2-10. a. LIPSS formed using the 1064 nm wavelength laser were also subjected to reflectance testing using the spectrophotometer. These results were also compared with FDTD simulations. The fill factor was measured

to be 75% and the depth of valleys was measured to be 350 nm. Once again a good

agreement between experimental and simulated results can be seen in Figure 2-10. b.
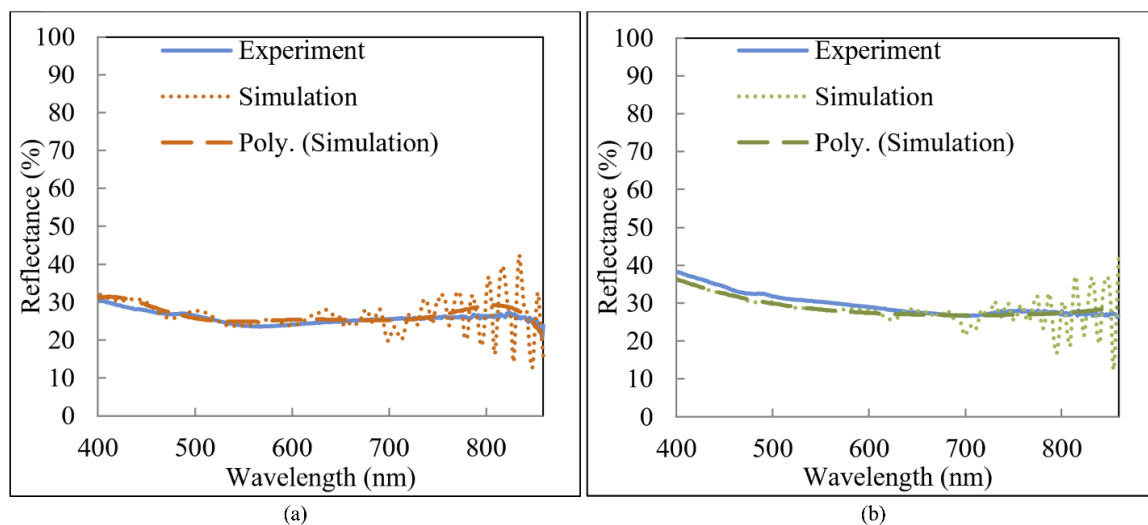
Figure 2-10. Comparison between experimental and simulated reflectance curves for
LIPSS having a period of a) 532 nm b) 1064 nm.

Simulations were conducted to study the effect on reflectance due to an oxide

layer on surface structures. It was found that the effects were negligible for oxide layers

smaller than 10 nm as seen in Figure 2-11. which shows the case of 532 nm period simple

grating with a valley depth of 300 nm. An oxide layer, if at all, present is not likely to

affect the average reflectance since it is expected to be very thin for such small exposure

times to high temperatures.
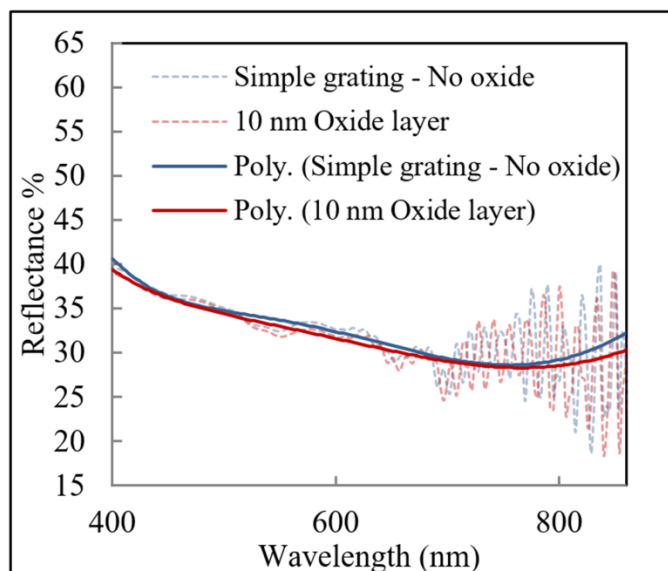
Figure 2-11. Reflectance curves for simple grating structures with and without an oxide layer.

Different grating profiles were compared through simulations to study their effects on reflectance. Four profiles were compared namely, a simple grating having a rectangular profile, grating with a rounded top, grating with an elliptical profile and a grating with a flat top having curved edges. These profiles were chosen as they were most similar to the experimental LIPSS obtained. Figure 2-12. shows the cross sectional view of the different profiles modeled. Although the profiles appear similar, their effect on reflectance varies significantly. The different profiles chosen were each simulated for multiple valley depths (varied from 200 nm to 400 nm in 50 nm intervals) and fill factors (varied from 55% to 75% in 5% intervals) and the results were analyzed. The elliptical profile resulted in the lowest average reflectance amongst the chosen profiles for all valley depths greater than 250nm and all fill factors. The gratings with flat tops having curved edges resulted in the highest average reflectance values. The cases of simple grating and round top gratings were intermediate to the previous two cases and were

dependent on the valley depth. For small valley depths of 200 nm to 250 nm, simple gratings provided lower average reflectance values while at higher valley depths of 300nm to 400nm, gratings with round top resulted in lower average reflectance. This can be seen in Fig. 10a) for the case of 65% fill factor.
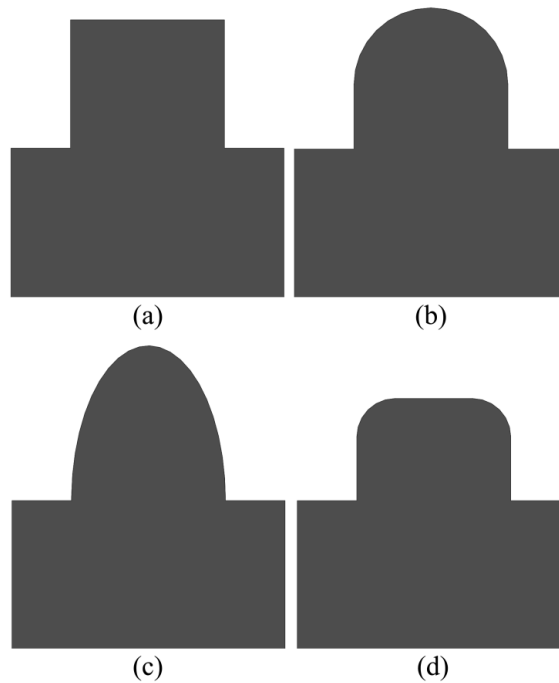
Figure 2-12. Profiles used in reflectance simulation a) simple grating b) rounded top c) elliptical profile and d) flat top with curved edges.

Simulations were also performed to study the effect of fill factor on the reflectance. The fill factor was varied from 50% to 80% in steps, by increasing the profile width while keeping the period and the depth of structures constant. This range was chosen as experimental data of LIPSS fill factors ranged between 60% and 75%. It was found that a fill factor of 50% was the most effective in suppressing surface reflectance. For fill factors higher than 50%, it was found that and as the fill factor was increased, the

average reflectance also increased as can be seen in Figure 2-13. b. Figure 2-13. b. shows

the case of a constant valley depth of 300 nm. For all profile types, there is an increase in

average reflectance with higher fill factors.

(a)

(b)

(c)
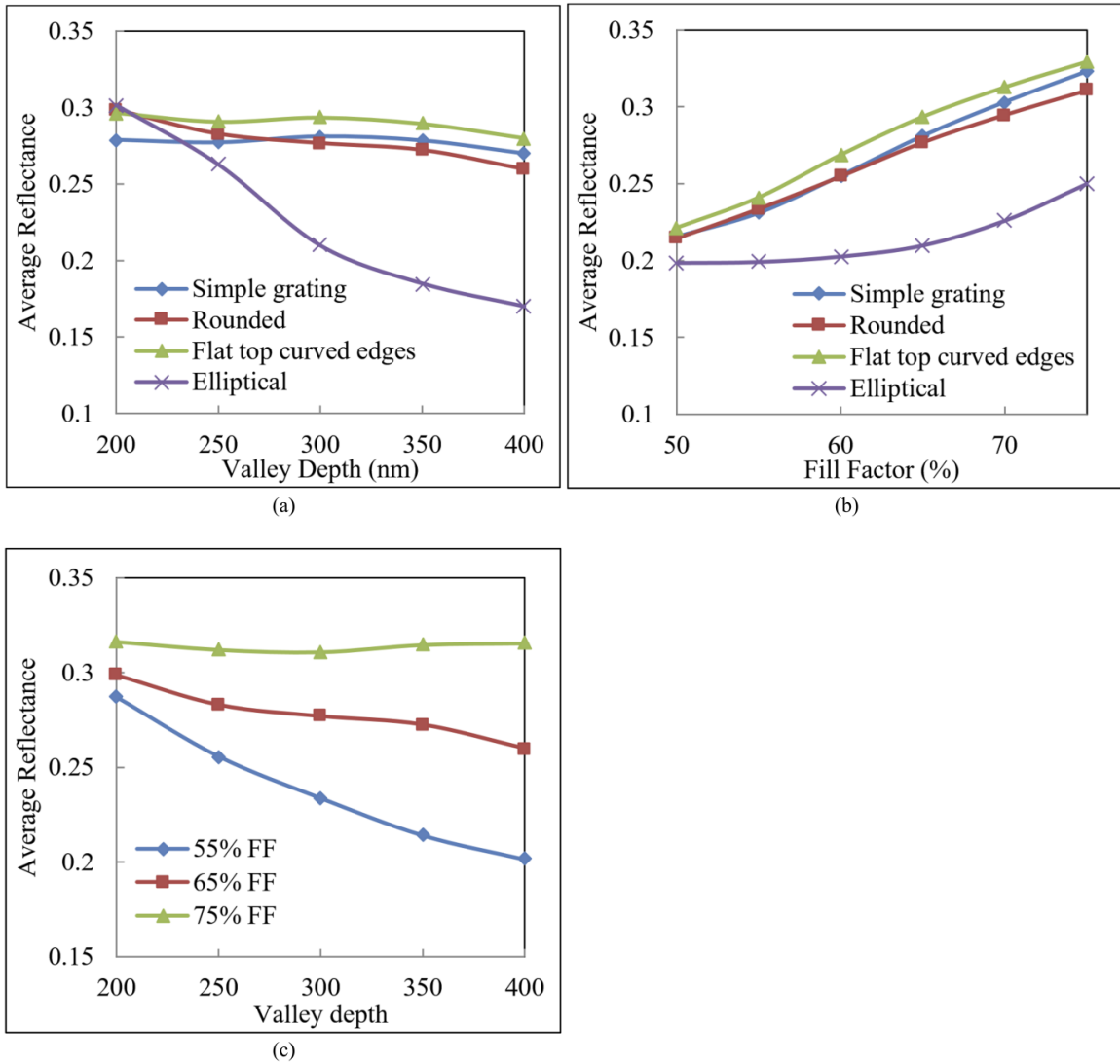
Figure 2-13. a) Average reflectance vs valley depth for different profiles for the case of 65% fill factor b) Average reflectance vs fill factor for different profiles for the case of 300 nm valley depth c) Sensitivity of average reflectance value to changes in valley depth for different fill factors.

The effect of changing the valley depth was also studied through simulations. The depth of the LIPSS valleys was varied from 200 nm to 400 nm in steps. This range was chosen as experimental data of LIPSS valley depths ranged between these values. It was found that the fill factor influenced the effect of changes in valley depth on the reflectance. At lower fill factors of 50% to 60%, deeper valleys resulted in lower reflectance values. This is explained by the fact that deeper valleys cause increased scattering and trap light more effectively. At slightly higher fill factors of 60% to 70%, a similar trend of decreasing average reflectance values with increasing valley depths was observed. However, it was observed that the average reflectance was less sensitive to changes in valley depth. At even higher fill factors ranging from 70% to 80%, the reflectance remained almost constant as the valley depth was increased from 200 nm to 400 nm. In some cases, even a small increase in average reflectance of up to 1% was observed over the wavelength range of 400 nm to 1100 nm. This is attributed to the fact that at high fill factors, the incoming light radiation is incident onto a larger front surface area as compared to the case of a lower fill factor. This would cause an increase in the surface reflectance. The sensitivity of average reflectance to increasing valley depth reduced as the fill factor increased as can be seen in Figure 2-13. c. Figure 2-13. c. represents the case of structures with a rounded top and the same trend was observed for all the different profiles simulated.

The simulations revealed that the ideal LIPSS for light trapping had a 450 nm period, a 50% fill factor and the deepest possible valleys. For a valley depth of 400 nm, the lowest simulated average reflectance was nearly 15% over the wavelength range of 400 nm to 900 nm. However, the average reflectance achieved experimentally was higher

than this value since the lowest achievable fill factor in experiments was 60% while the lowest achievable period was around 500 nm. Also, to avoid material ablation associated with higher fluence values, the valley depth was limited to below 400 nm. By using a lower wavelength laser, the optimal period can be achieved which will result in a further reduction in average reflectance.

The drop in reflectance in silicon textured with optimized LIPSS is comparable with that of single layer ARCs. The highest drop in average reflectance in the wavelength range of 400 nm to 1100 nm for silicon solar cells using single layer ARCs is from 40% down to around 15%. In the case of an optimized double layer ARC this value decreases to around 7% [110]. However, the time and cost involved in coating solar cells with ARCs is very high making LIPSS texturing a viable alternative to using ARCs.

2.3   LIPSS on CIGS Thin Film Solar Cells

In order to improve the efficiency of Copper Indium Gallium Selenium (CIGS) thin film solar cells, a similar approach to the one discussed in the case of silicon solar cells was applied. Unlike silicon solar cells, the CIGS thin film solar cell consists of several layers stacked on top of each other. The total cell thickness is of the order of a few microns. Figure 2-14. shows the construction of a typical CIGS solar cell.
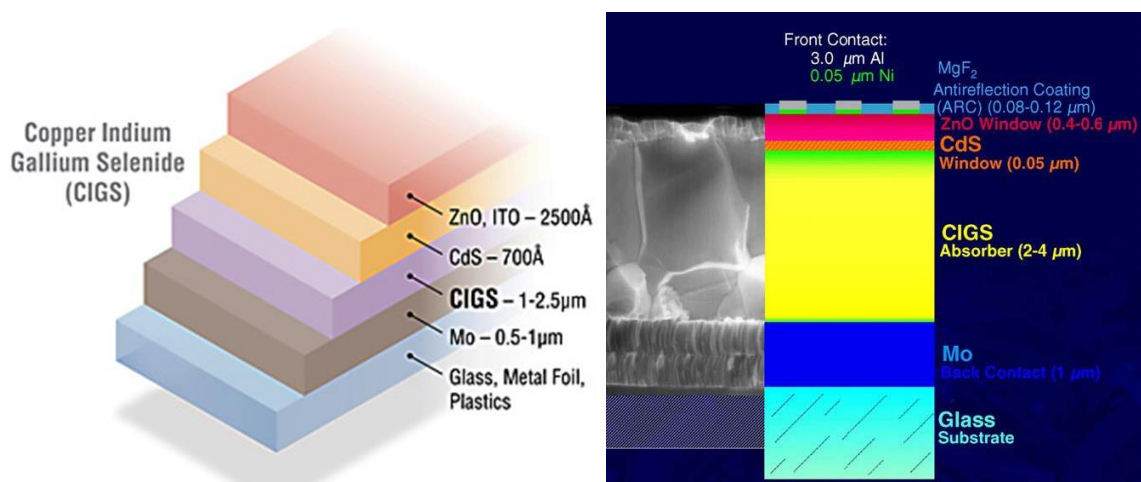
Figure 2-14. a) Layers in a typical CIGS thin film solar cell [111] b) Cross section image of a CIGS thin film solar cell [112].

In order to maximize light trapping in the CIGS thin film solar cell, it was decided to texture the CIGS absorber layer. Since the absorber layer is below the CdS and ZnO layer in completed thin film solar cell, an incomplete cell without the upper layers added was obtained from the industry. FDTD simulations were run to determine the ideal LIPSS period and height to minimize surface reflectance. A period between 550 nm and 750 nm was found to be ideal for light trapping in the desired wavelength range of 300 nm to 1100 nm. A Ti:Sapphire femtosecond laser was used to irradiate the surface. A repetition rate of 1 KHz was used and the pulse width was 100 fs.

Parameters were identified to create LIPSS on the CIGS absorber layer. Initial experiemtns were conducted to determine the laser fluence required to create LIPSS on the surface of CIGS without ablating the entire layer. The spot size was set to 60 µm and the speed was set to 0.5 mm/s. Initially a high fluence of 2 J/cm^2 was used. This caused the top layers of the cell to be ablated exposing the stainless steel back plate. During this process, LIPSS were created on all layers of the cell as seen in Figure 2-15.
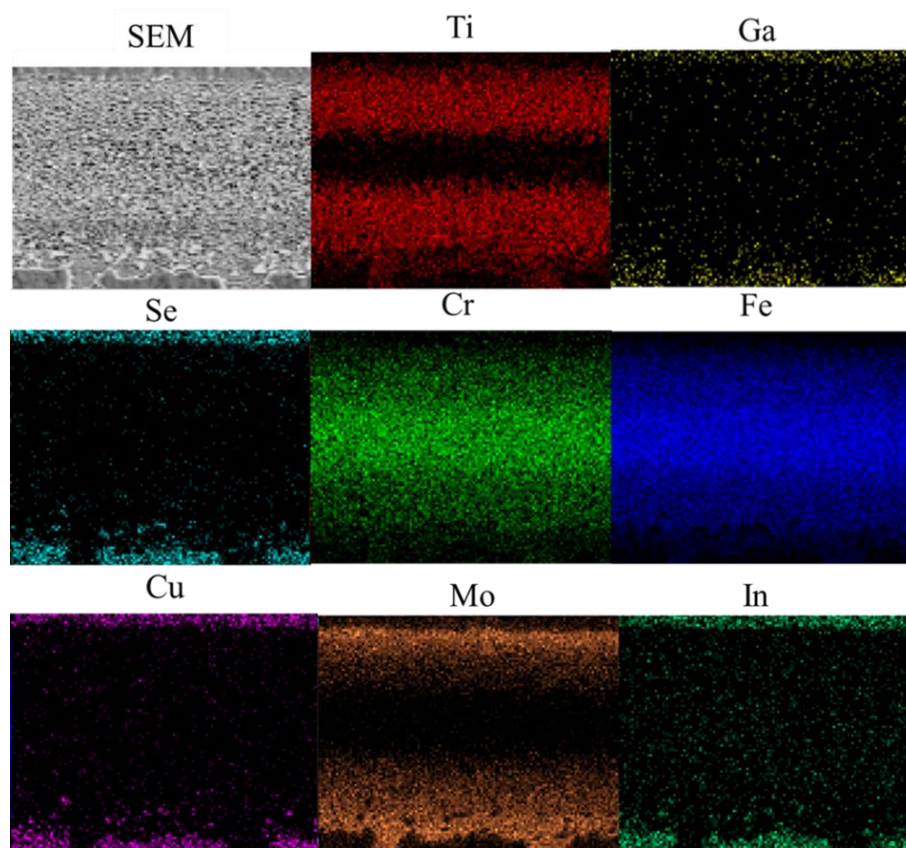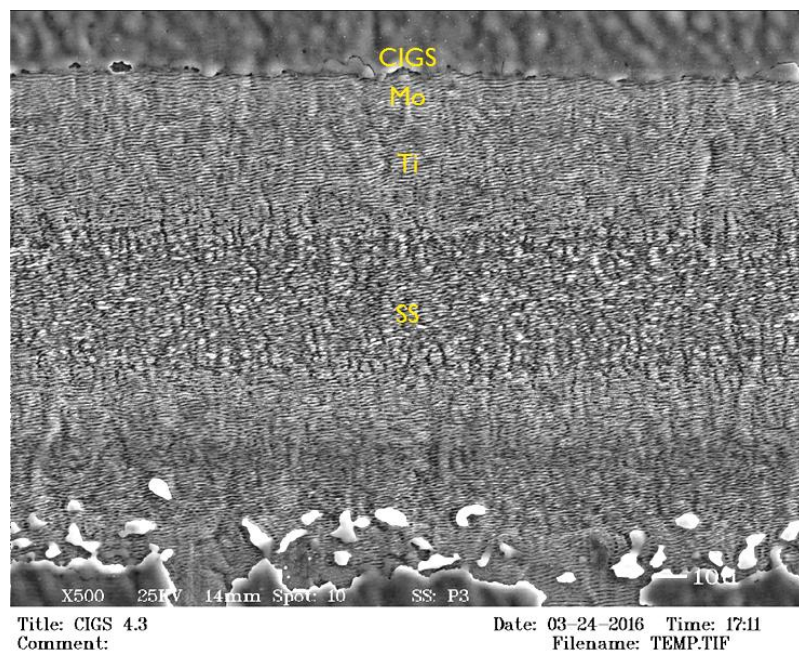
Figure 2-15. SEM image (above) and X ray map (below) of LIPSS created on various layers of a CIGS thin film solar cell.

The fluence was reduced to below 1 J/cm^2 to prevent ablation of the CIGS layer. Since the original CIGS surface was rough due to the manufacturing process involved in depositing the layer, two laser scans were used to generate LIPSS on the surface. The first pass was used to melt and flatten the CIGS crystals to obtain a smooth surface for LIPSS formation. It was found that two laser scans each at the fluence of 0.9 J/cm^2 were ideal to create uniform LIPSS on the CIGS surface as seen in Figure 2-16. The LIPSS period was measured to be nearly 650 nm.
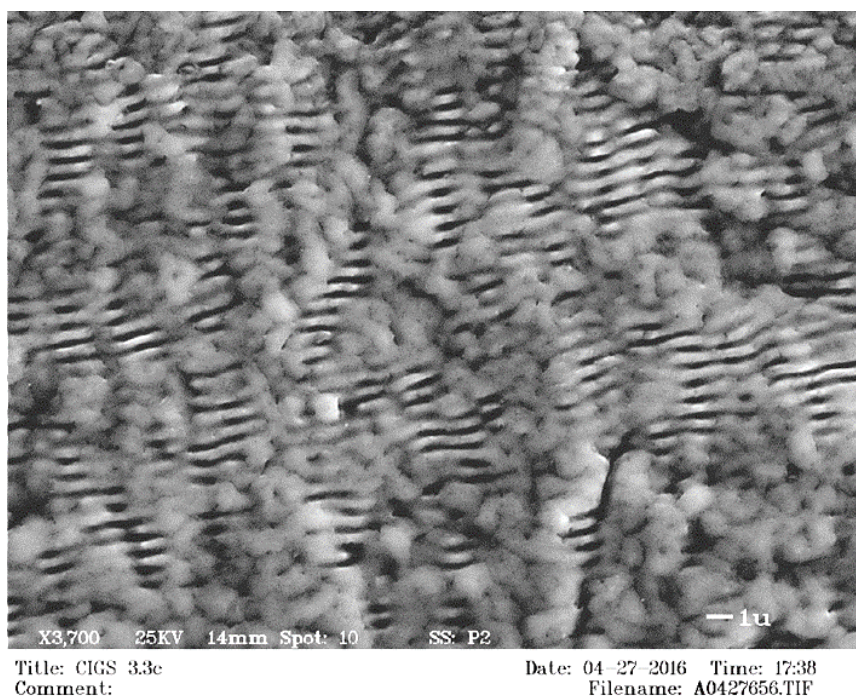
Figure 2-16. Uniform LIPSS created on the CIGS absorber layer.

The textured CIGS surface was tested for surface reflectance using a spectrophotometer as was discussed in the case of silicon earlier. This data was compared with the FDTD simulation results for LIPSS with a fill factor of 65% a depth of 300 nm and a period of 650 nm. The results are seen in Figure 2-17.
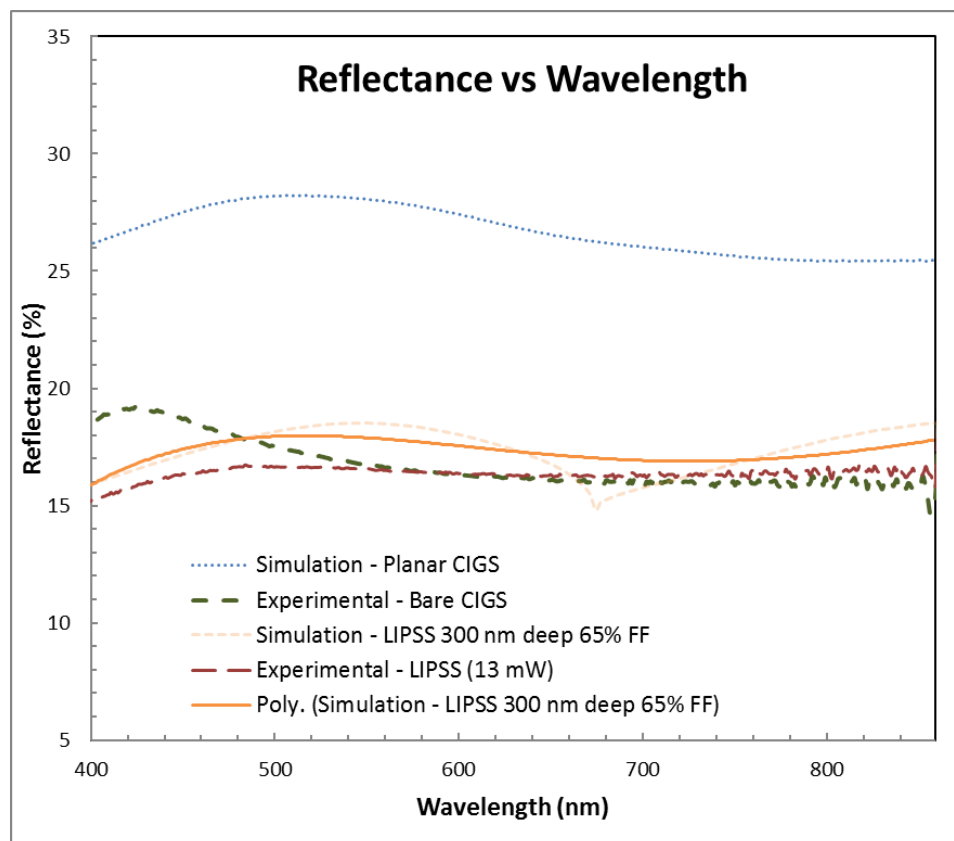
Figure 2-17. Reflectance vs wavelength curve showing simulated and experimental data for CIGS textured with LIPSS.

The simulation results matched the experimental data well. The average reflectance was reduced by 10% as compared to perfectly flat CIGS. However, since the initial surface of CIGS was also rough, a net improvement of only 0.4% was observed from the rough surface to the LIPSS textured surface, making the process uneconomical for industrial use.

2.4   Summary

By utilizing the light trapping properties of periodic grating structures, silicon wafers with average reflectance values of 23.1% were fabricated by texturing the surface with a

picosecond laser. These structures were created at high laser scanning speeds of 4000 mm/s and low pulse overlapping ratios of 60%. This method provides an inexpensive and rapid process to create low reflectance silicon wafers which can be used in photovoltaic applications. Although there have been many studies on the anti-reflective properties of LIPSS [113] created by femtosecond lasers, little work has been done in this area using picosecond lasers. Moreover, LIPSS formed by a picosecond laser has not been reported at high scan speeds exceeding 3000 mm/s, which is an important attribute to lowering the fabrication costs of solar cells. In addition, the anti-reflective properties of large area LIPSS created with low overlapping ratios of less than 65% have been rarely reported, which were addressed in this work. A decreasing trend in average reflectance was observed when the LIPSS were created with increasing fluence values up to 1.4 J/cm^2. Beyond this value material ablation was observed. The experimentally achieved reflectance values for highly periodic LIPSS have been validated through FDTD simulations that displayed a high degree of predictability. Various periodic geometries were simulated to study their impact on surface reflectance. Elliptical profiles resulted in the lowest average reflectance amongst the profiles simulated. The effects of changing valley depth and fill factor in each of these structures were also studied, showing that higher fill factors resulted in higher average reflectance values. A steady drop in sensitivity of average reflectance to change in valley depth is reported as the fill factor is increased above 50%. The results presented provide guidelines for optimal design of periodic structures for light trapping in silicon solar cells.

CHAPTER 3. SUPERHYDROPHOBIC SURFACE STRUCTURES

3.1   Experimental Details

A Ti-Sapphire femtosecond laser (Spectra Physics - Spitfire Pro) was used to create superhydrophobic surface structures on metal surfaces as seen in Figure 3-1. The laser generates a linearly polarized Gaussian beam with a wavelength of 800 nm. The pulse width is 100 fs with a pulse repetition rate of 1 kHz. The set up consisted of a half wave plate and a thin film polarizer to control the power output. A high speed shutter was used to control the laser beam for marking. This was followed by a quarter wave plate to achieve circular polarization. The beam was focused using a 45 mm focal length objective lens. A high precision nano positioning 3 axis computer controlled stage (Aerotech ANT130-XY and ANT130-5-V) was used to mount and position the target sample in the laser beam focal plane.
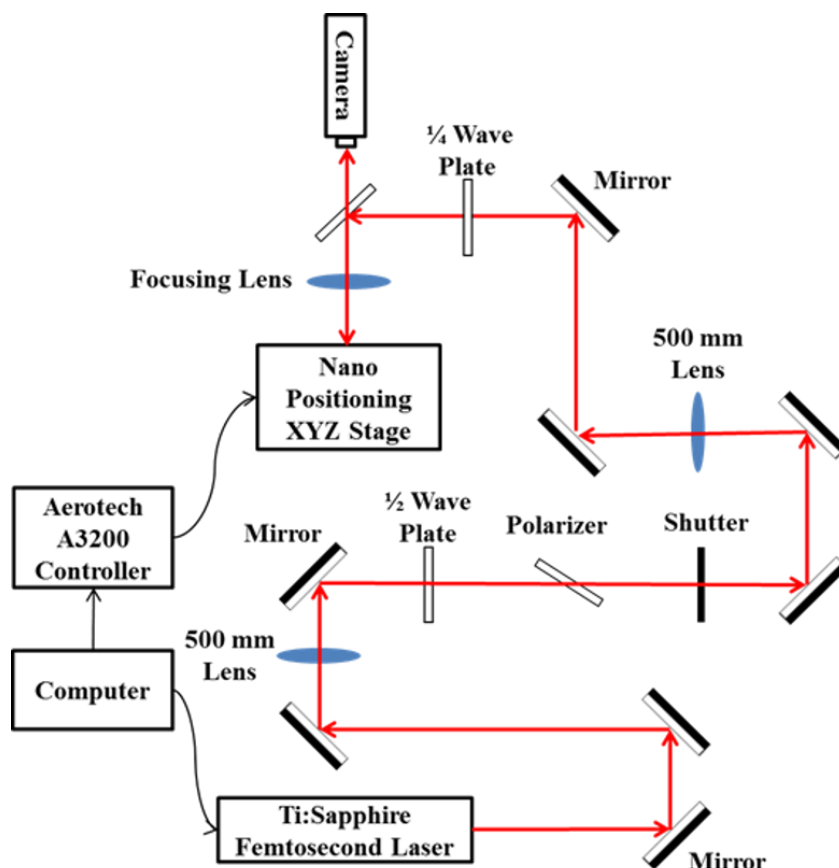
Figure 3-1. Femtosecond laser setup used to create hydrophobic surface structures.

3.1.1 Nanostructure transfer to polymers

Copper was used as the metallic sample in the study due to its excellent formability. The sample thickness was chosen to be 50 µm for its ease of handling and forming. Initial experiments were conducted to determine if nanostructures would successfully transfer from the metal surface onto PDMS. To evaluate the possibility of transferring the nanostructures from a metallic surface to PDMS, the copper surface was textured with laser induced periodic surface structures (LIPSS) using femtosecond laser pulses. The laser fluence was varied in the range of 4 J/cm^2 and 12 J/cm^2 while maintaining a 90% overlapping ratio, to create LIPSS of varying depths. The textured

surface was imaged under the SEM. The LIPSS period was measured to be between 670

nm and 700 nm while the depth varied between 300 nm and 500 nm. PDMS base, mixed

with the curing agent was poured onto the textured surfaces and allowed to cure,

following which, the PDMS was peeled off the surfaces of the metals. Since PDMS is

non-conductive, the surface was sputter coated with platinum before SEM imaging to

create a conductive top layer to prevent sample charging. However, it was found that due

to the flexibility of PDMS, the sputter coated platinum layer was broken and cracked

easily, making SEM imaging difficult. In order to study the surface of PDMS, an

environmental SEM was used at low vacuum. This allowed imaging of the non-

conductive PDMS without a conductive coating. It was found that the surface nano

structures were successfully transferred onto PDMS with no damage to the surface

features as seen in Figure 3-2. The details of the surface were maintained and the PDMS

surface was found to replicate the copper surface.
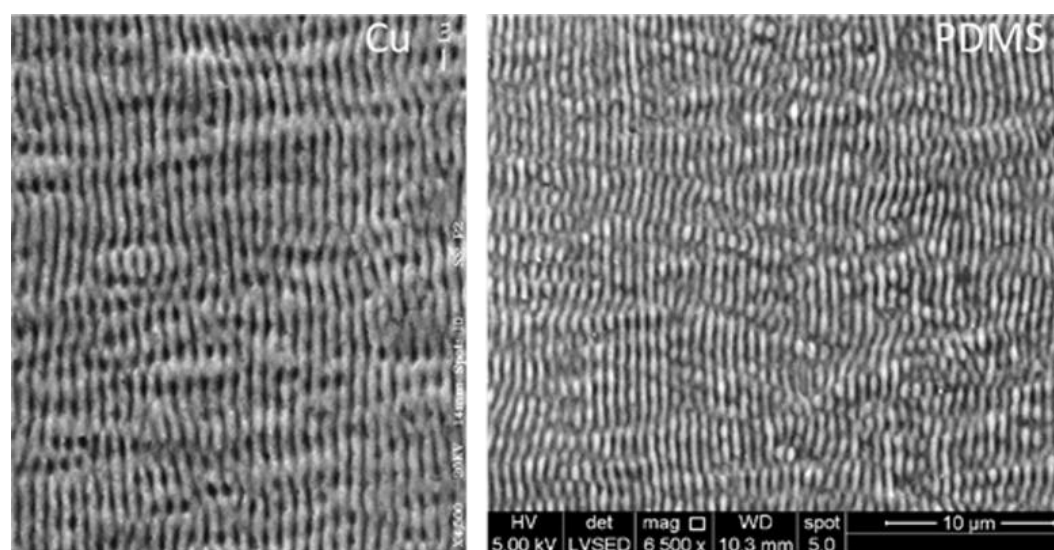
Figure 3-2. LIPSS created on the surface of copper (left) and transferred onto PDMS
(right) using transfer molding.

3.2   Femtosecond Laser Surface Structuring

3.2.1   Surface nano structures

Hydrophobic surface structures were created on copper and transferred to PDMS to increase the water contact angle and reduce contact angle hysteresis. Initial experiments were conducted to study the effects of LIPSS and random nano roughness on the surface wettability of copper and PDMS. The textured copper and PDMS surfaces were tested for water contact angle using an automated goniometer. For each type of nano structure created, the contact angle achieved for copper and PDMS are shown in Figure 3-3. and Figure 3-4. as inserts. The parameters used to create each surface structure and the corresponding contact angle values achieved on copper and PDMS are discussed below.

In order to study the effect of periodic nano structures, LIPSS were created on the surface of copper by varying the femtosecond laser fluence between 4 J/cm^2 and 20 J/cm^2. A 50 µm spot size was used and parallel scans were made 40 µm apart. A scan speed of 15 mm/s was used resulting in a pulse overlapping ratio of 70%. The resultant LIPSS had a period of 700 nm and a depth between 300 nm and 500 nm. These structures were completely transferred onto PDMS. For fluence values lower than 10 J/cm^2, the surface of the textured copper appeared iridescent due to the grating effect of shallow LIPSS. As the fluence was increased beyond this value the appearance became dull and eventually darker. This is attributed to the light trapping nature of LIPSS which is amplified as the depth of features increases. The SEM and ESEM images of the copper and PDMS surfaces respectively are shown in Figure 3-3. The highest water contact

angle of 147° was measured on the surface of copper textured with LIPSS using a fluence

value of 14 J/cm^2. The corresponding PDMS surface resulted in a contact angle of 125°.

The goniometer images of water droplets on the surfaces of copper and PDMS are also

shown in Figure 3.
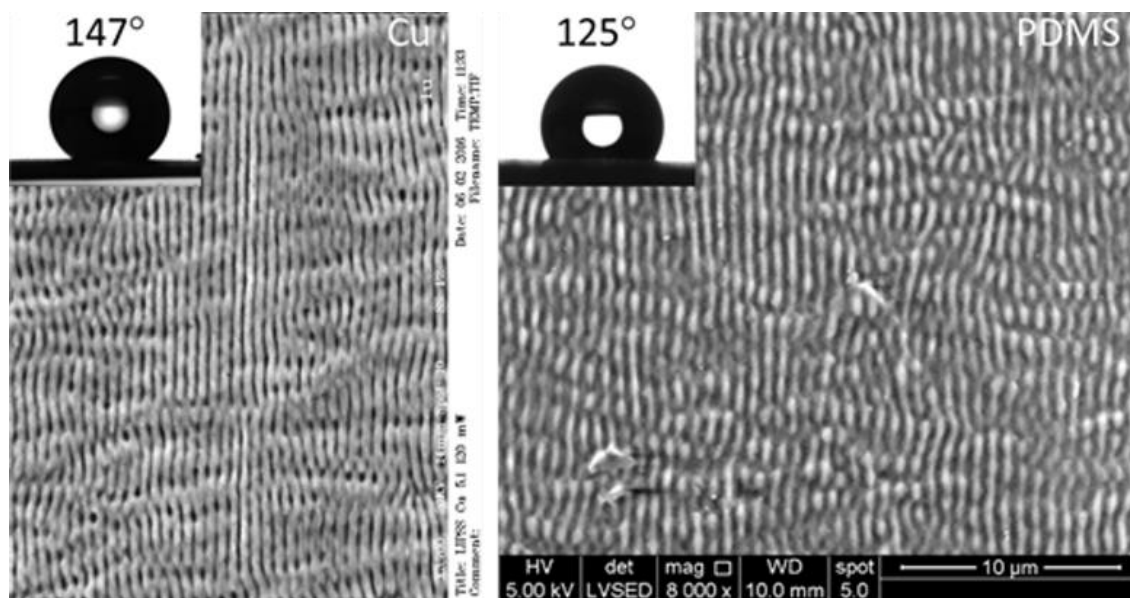
Figure 3-3. LIPSS created on copper showing a water contact angle of 147° (left) and on
PDMS showing a contact angle of 125° (right).

The LIPSS textured surface was compared with a surface covered in random nano

bumps. In order to create a surface covered with nano scale roughness, the fluence used

was in the range of 60 J/cm^2 and 100 J/cm^2. The surface was scanned in a grid pattern at a

scan speed between 1 mm/s and 2 mm/s with a 10 µm spacing between adjacent passes.

These structures were transferred onto PDMS as can be seen in Figure 4. The highest

contact angle achieved in the case of copper was 148° while PDMS showed

superhydrophobicity with a contact angle of 151°. The roll off angle for this surface,

however, was nearly 40° making it unsuitable for drag reduction applications. From these

results it was observed that nano bumps were more effective in increasing the contact angle as compared to periodic ripples. This is attributed to the fact that the surface area in contact with the liquid is minimized in the case of random nano roughness leading to reduced forces of adhesion at the interface.
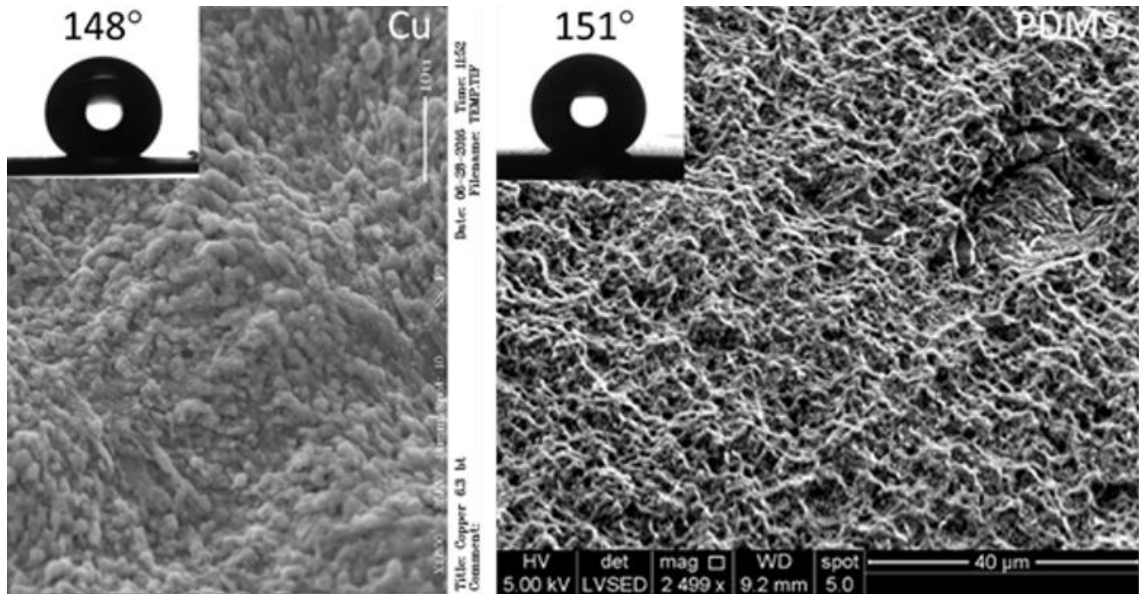
Figure 3-4. Nano roughness created on copper showing a water contact angle of 148° (left) and on PDMS showing a contact angle of 151° (right).

3.2.2 Dual scale micro/nano surface structures

Nano structured surfaces were found to increase the contact angle but due to the high contact angle hysteresis observed on these surfaces, the roll off angles were high. This is undesirable for surface drag reduction applications. In order to reduce the hysteresis, dual scale features were created to promote the Cassie Baxter state of wetting. It was decided to create convex microstructures covered with smaller nano scale features. Multi scale features were used to reduce the size of features required to achieve

superhydrophobicity. The largest feature height was limited to 15 µm above the surface. The aspect ratio and spacing between features were varied to optimize the water contact angle. Various surface structures were created on the copper surfaces using femtosecond laser pulses as shown in Figure 3-5. and Figure 3-5. These structures were transferred onto PDMS and the water contact angles were measured using the goniometer.

3.2.2.1   Micro grooves

Parallel micro grooves with nano LIPSS were created as seen in Figure 3-5. a. Parallel scans were made on the surface of copper and the fluence was varied between 80 J/cm^2 and 120 J/cm^2. The spacing between channels was varied between 10 µm and 50 µm and the overlapping ratio between 75% and 90%. The highest contact angles were achieved for a spacing of 25 µm and a fluence value of 95.5 J/cm^2. The features were measured to be 8 µm in height. The PDMS replica showed some micro bumps on top of grooves due to the valley texture of the copper grooves. This resulted in a 147.5° contact angle with a low roll of angle under 8° in the case of PDMS.

By increasing the fluence and varying the overlapping ratio between 90% and 95%, microchannels with nano bumps were created on copper as seen in Figure 3-5. b. The highest contact angles were achieved for a groove spacing of 25 µm and a feature height of 10 µm. These structures were also found to be highly hydrophobic and exhibited contact angles of over 160° in the case of copper and over 140° in the case of PDMS. The PDMS replica showed slightly different top surface nano structures due to a difference in the valley texture in the copper grooves. This resulted in a lower contact angle of 143° in the case of PDMS. A low roll off angle of less than 5° was observed for

this structure on copper. The roll off angle on PDMS was slightly higher but was found to be under 10°. In both the cases of micro grooves, it was observed that nano bumps are more effective in increasing the contact angle and reducing hysteresis as compared to nano ripples.


Figure 3-5. (a) Micro-grooves with nano-ripples created on copper showing a water contact angle of 158.1° (left) and on PDMS showing a contact angle of 147° (right), (b) Micro-grooves with nano-bumps created on copper showing a water contact angle of 162° (left) and on PDMS showing a contact angle of 143° (right).

3.2.2.2   Micro bumps

In order to further reduce the contact area of water on the surface and enhance the Cassie Baxter state of wetting, micro bump features were created on the surface of copper. Micro bumps covered with nano scale LIPSS were created by scanning the surface in the shape of a grid with lines normal to each other. A spot size of 20 µm was used and the spacing between scan lines was varied between 10 µm and 50 µm to achieve different micro bump profiles. The surface features were varied by changing the fluence between 15 J/cm^2 and 40 J/cm^2. High overlapping ratios of 90% to 95% were used. These structures were completely transferred onto PDMS as seen in Figure 3-6. a. The highest contact angles achieved were 157°on copper and 126° on PDMS and corresponded to a spacing of 30 µm and a fluence of 32 J/cm^2. The micro bumps were measured to be 8 µm in height. The LIPSS on the surface had a period of 700 nm and a height of nearly 400 nm.

As in previous cases, varying the nano scale features on the surface was expected to change the wettability of the surface. Instead of nano ripples, nano bumps were created on the surface of micro features by varying the fluence between 80 J/cm^2 to 200 J/cm^2 and the overlapping ratios between 75% and 90%. These structures were transferred onto PDMS as seen in Figure 3-6. b. Both the copper and PDMS surfaces were found to behave superhydrophobic. The highest contact angles achieved were 165°on copper and 153° on PDMS and corresponded to a spacing of 25 µm and a fluence of 95.5 J/cm^2. The features were measured to be 12 µm in height while the nano bumps were found to range from 100 nm to 1 µm. The contact angle hysteresis was found to be very low for this structure leading to low roll off angles of less than 5° on both copper and PDMS. Once

again it was observed that nano bumps were more effective in increasing the contact

angle and reducing the contact angle hysteresis.
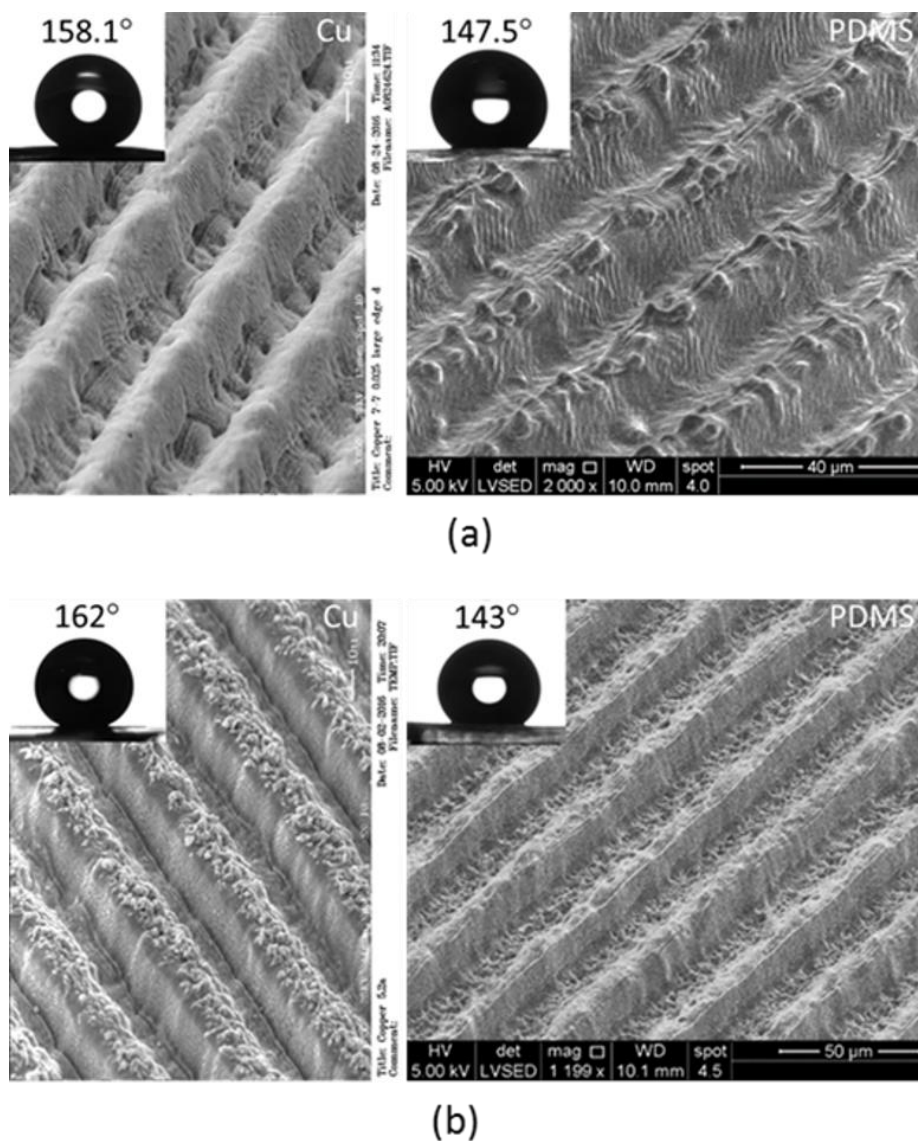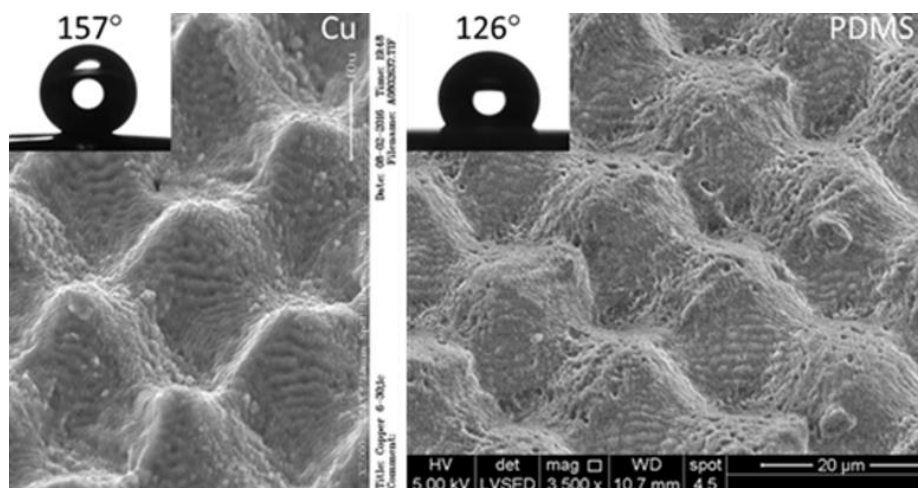

Figure 3-6. (a) Micro-bumps with nano-ripples created on copper showing a water contact angle of 157° (left) and on PDMS showing a contact angle of 126° (right), (b) Micro-bumps with nano-bumps created on copper showing a water contact angle of 165° (left) and on PDMS showing a contact angle of 150° (right).

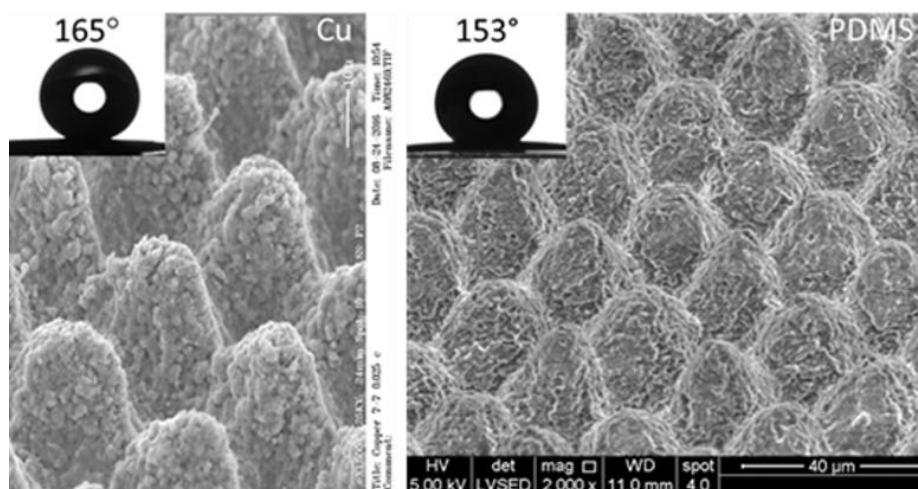Table 3.1. Summary of contact angle (CA) values for different surface structures.

Surface structure	CA Copper (°)	CA PDMS (°)
LIPSS	147	125
Nano roughness	148	151
Micro grooves with nano ripples	158	147.5
Micro grooves with nano bumps	162	143
Micro bumps with nano ripples	157	126
Micro bumps with nano bumps	165	153

The water contact angles of the textured surfaces are summarized in Table 3.1. Summary of contact angle (CA) values for different surface structures. The highest contact angles of 165° for copper and 153° for PDMS were achieved in the cases of microbumps with a spacing between 25 µm and 30 µm created at a fluence of 95 J/cm^2. A high contact angle was also achieved on surfaces textured with micro grooves with nano ripples having a spacing of 25 µm created at a fluence of 95 J/cm^2. Based on these results it can be concluded that nano scale features play an important role in determining the wettability of a surface. In all cases, nano bumps were found to be more effective than nano ripples in enhancing the surface wettability. It can also be concluded that various contact angles can be achieved on both metals and polymers by varying the surface geometry. This can be used in several applications including controlling fluid flow in

microfluidics as will be discussed in subsequent sections. Several other surface structures were created on the surface of copper. The SEM images these surface textures and their corresponding contact angle measurements can be seen in the Appendix.

It was observed that the contact angle of copper was reduced, immediately after laser texturing. This is attributed to the fact that copper is inherently hydrophilic and the surface roughness leads to an increase in this hydrophilicity. However, after PDMS is poured on the surface for the texture transfer, silanization of the copper occurs, making it highly hydrophobic. It was also observed that the samples which were not treated with PDMS, when exposed to the ambient atmosphere for 10 to 15 days, eventually exhibited hydrophobicity. This is attributed to the addition of low surface energy carbon groups to the textured surface due to the decomposition of atmospheric CO_2. The contact angle measured on copper samples exposed to the atmosphere for 15 days, were found to be similar to the contact angles achieved on copper immediately after the PDMS transfer.

3.3   Fabrication and Testing of Textured Microfluidic Devices

One of the many potential applications of superhydrophobic polymer surfaces is in microfluidics. The flow rate of fluids through micro-channels is an important parameter in the design of microfluidic devices. Chemical treatment is commonly used to change the wettability of microfluidic channel inner walls to vary the flow rate. As discussed earlier, there are limitations to using chemical treatments to vary the wettability of micro fluidic channel walls. The process discussed below allows the fabrication of

textured hydrophobic microfluidic inner channel walls. This reduces the fluid drag at the microchannel walls and therefore allows control over the flow rate through the channel.

In order to create superhydrophobic inner walls in PDMS microfluidic channels, metallic molds were created using aluminum blocks as seen in Figure 3-7. a. The final microfluidic channel diameter was chosen to be 200 µm. Therefore, the mold channel was made 300 µm in diameter to compensate for the 50 µm thickness of the copper foil. The molds were designed to accommodate for the inlet and outlet ports of the microfluidic device. Different micro end mills were used to create the channel and the outlets. The molds were used to mechanically form 50 µm thin copper foil into the desired channel shape. The formed copper foils were textured using the femtosecond laser and placed in a petri-dish as seen in Figure 3-7. b. Micro bumps with nano bumps were chosen as the surface structure to achieve superhydrophobicity in the channels due to the high contact angles and low roll off angles achieved with these structures. These structures were selected to reduce the drag produced due to adhesive forces on water flowing inside the channel. The parameters used to create these surfaces were similar to the parameters discussed in section 3.2.2.2. The textured channels were used as molds and PDMS was poured onto the textured foil. The cured PMDS was peeled off to reveal micro channels in the surface with textured inner walls. This formed one half of the micro fluidic device while and a second half was fabricated by the same process. The two PDMS halves were bonded together to form a completed microfluidic device as seen in Figure 3-7. c. A small amount of PDMS curing agent was used between the two halves which were aligned together and allowed to form a strong bond. Samples were prepared having both textured and un-textured channels but the channel length and diameter were

kept contact in both cases. Needles with tubing were used to supply water to the devices

to measure fluid flow. The textured copper and PDMS channels were imaged using an

SEM and ESEM as seen in Figure 3-8. a and Figure 3-8. b respectively. A 3D optical

profiler was used to image the copper channel as seen in Figure 3-8. c.
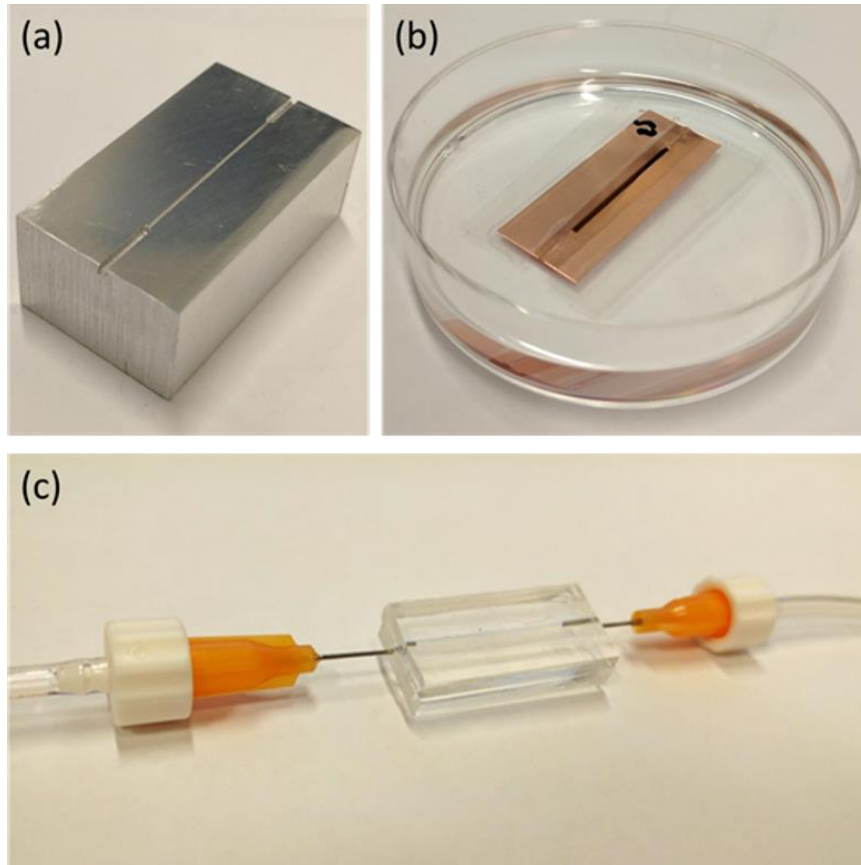
Figure 3-7. (a) Micro machined Aluminum microchannel mold, (b)Formed and textured copper foil immersed in PDMS, (c) PDMS microfluidic device with fluid inlet and outlet connections.
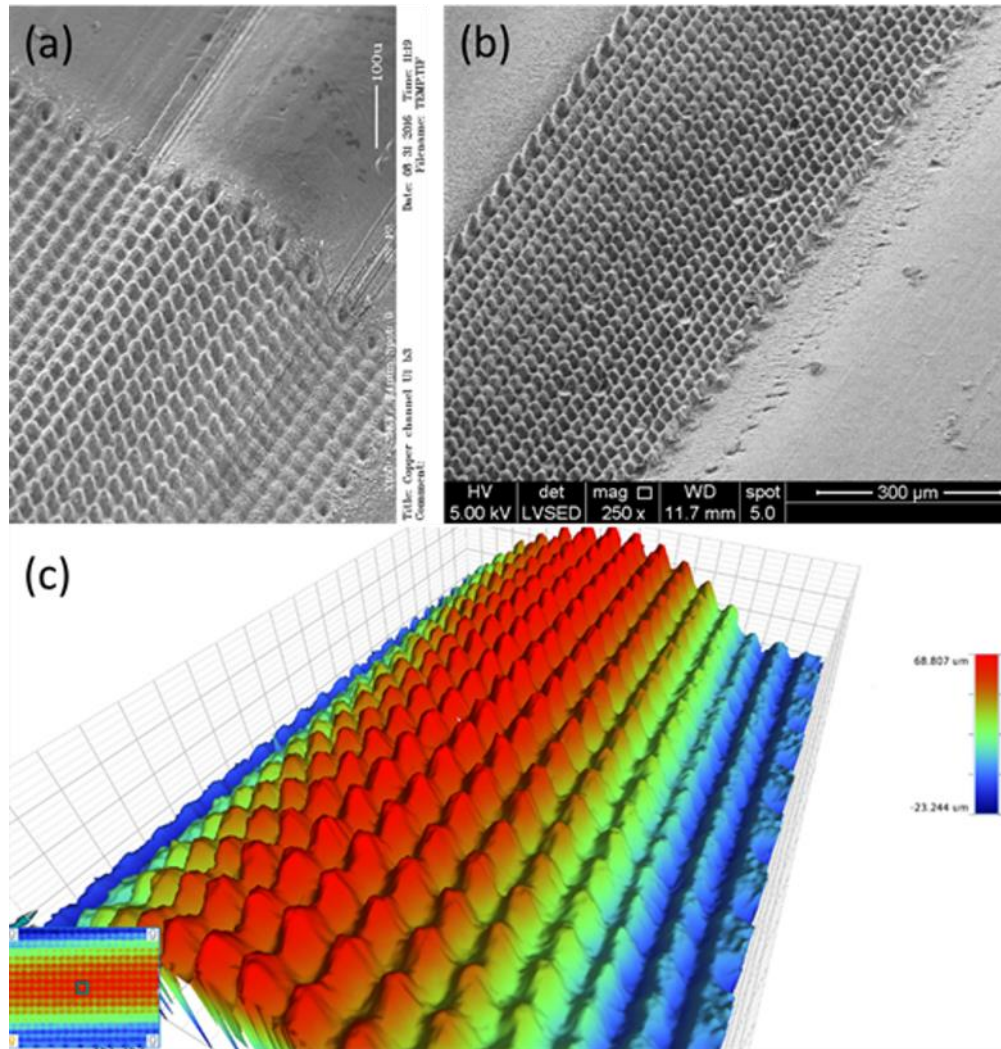
Figure 3-8. (a) SEM image of formed and textured copper microchannel, (b) ESEM image of transferred PDMS microchannel, (c) 3D optical profiler image of a textured copper microchannel.

In order to compare the flow rate through the textured and un-textured devices, water was supplied through both devices at a constant pressure. A common pressure source was used and a bifurcation in flow was created to supply fluid at an equal pressure to both devices. The flow rate through the device was calculated by collecting fluid at the outlets of the two devices for a fixed period of time and weighing the fluid collected at each outlet using a high precision weighing scale. A color dye was supplied through the

channels to identify leaks in the devices. Several trials were run and it was found that in

the case of the un-textured device, an average flow rate of 0.773 ml/min was achieved.

For the same constant input pressure, the average flow rate though the textured sample

was found to be 2.227 ml/min as seen in Figure 3-9. Therefore, a 186% increase in flow

rate was achieved by texturing the inner walls of the microfluidic channel. The higher

flow rate through the textured sample is attributed to the reduction in drag due to the

superhydrophobic inner walls. By varying the hydrophobicity of the inner channel walls

using different surface structures, the drag can be controlled accurately to achieve the

desired flow rate through channels.

Figure 3-9. Flow rate measurements through textured and un-textured microfluidic
channels.

This process can be used in applications where the resistance to flow though

micro channels is to be reduced or controlled. Some examples of such applications are in

fluid supply tubing, controlled mixing of fluids, syringes etc. Surface structures which help achieve high contact angles but also high contact angle hysteresis as seen in section 3.2.1 can be u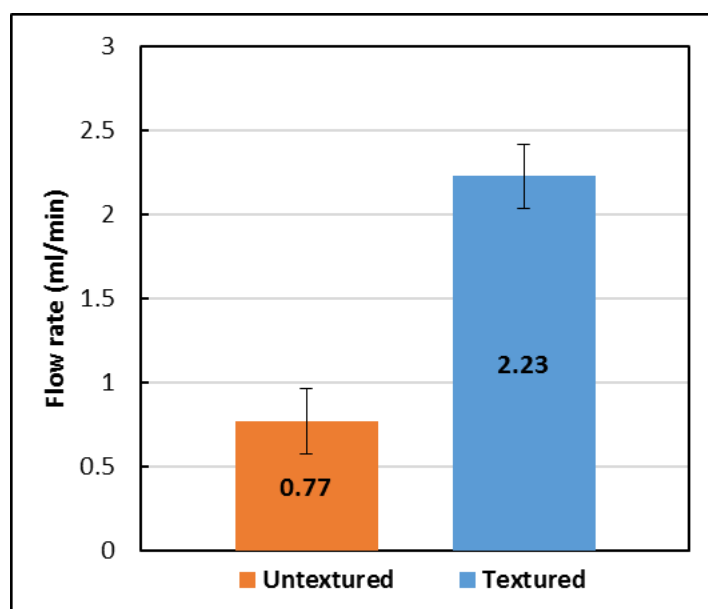sed to restrict flow through channels. This can be used to create flow control valves in microfluidic devices. A byproduct of this process is superhydrophobic copper. Although the copper surfaces turn superhydrophobic by exposure to ambient atmosphere, the PDMS treatment makes this process faster. The superhydrophobic copper surfaces can be used in applications such as MEMS, compact heat exchangers to increase thermal efficiency, water resistant electronics, drag reduction etc.

The die is not damaged during the transfer process and can be reused. A single die can be textured and used to fabricate multiple microfluidic devices.

3.4   Summary

Various surface structures were designed and created on the surface of copper using femtosecond laser pulses with the objective of increasing the water contact angle and decreasing the contact angle hysteresis. Surface nano structures were found to have a strong impact on the contact angle of microstructured surfaces. Nano bumps were found to be more effective in increasing the contact angle as compared to periodic nano ripples for the same surface micro structure. Surfaces textured with micro bumps covered with smaller nano bumps were found to be the most effective in increasing water contact angle and achieving superhydrophobicity. These surface textures resulted in water contact angles over 165° and contact angle hysteresis less than 5° in the case of copper. The structures were transferred onto PDMS through transfer molding to achieve

superhydrophobic PDMS surfaces with a water contact angle of over 153°. The metal and

polymer replica showed similar trends in wettability with changing surface structures.

 A process to create microfluidic channels with superhydrophobic inner channel walls

was described in detail. Formed and laser textured copper foils were used as

microchannel molds and transferred to PDMS via transfer molding. The hydrophobicity

of the inner wall surfaces is controllable through surface structure and can be used to

reduce drag and vary the flow rate through microfluidic devices. By creating dual scale

superhydrophobic surface structures on inner channel walls, the fluid flow rate through

PDMS microfluidic devices was increased by 186% compared to un-textured devices.

CHAPTER 4. CONCLUSIONS AND FUTURE WORK

4.1   Conclusions

Laser surface texturing has several advantages over other surface texturing methods. It has wide ranging applications, some of which were explored as part of this work.

1. Laser surface texturing was used to create LIPSS on the surface of silicon to improve its optical properties for solar cell applications. The surface reflectance of silicon was reduced from 40% to under 20% over the wavelength range of 400 nm to 850 nm by creating light trapping LIPSS. The lowest reflectance was achieved in the case of LIPSS with a period of 532 nm and a feature depth of around 350 nm created at a fluence of 1.4 J/cm^2.

2. Uniform LIPSS can be created at a high speed by reducing the pulse to pulse overlapping ratio. A 60% pulse overlap ratio was found to be the lowest achievable overlap while still creating uniform and continuous LIPSS.

3. FDTD computer simulations of LIPSS reflectance matched closely with experimental results showing high predictability. The lowest simulated silicon reflectance value of 15% was observed in the case of LIPSS with an elliptical profile. The optimal LIPSS period was found to be 450 nm and the optimal fill factor was found to be 50%

4. Nano structures such as LIPSS were transferred from the surface of metals to polymers using transfer molding. This shows that it is possible to completely and accurately transfer surface structures from metal surfaces to polymers down to the nano scale. This can be used to create structures on polymers which are otherwise difficult to produce by direct laser texturing.

5. A wide range of contact angles and contact angle hysteresis values can be achieved by changing surface micro and nano structures independently. The impact of nano structures on wettability of microstructured surfaces was found to be significant and the nano structures strongly influenced the contact angle and contact angle hysteresis of the microstructured surface.

6. The highest contact angle of 165° with a CAH value of under 5° was achieved by creating micro bumps with nano bumps on the surface of copper. This surface when transferred to PDMS resulted in a contact angle of 153° and a contact angle hysteresis of less than 5°.

7. Microfluidic devices can be fabricated by transfer molding. This process allows the creation of micro and nano scale features on the inner channels of the device which can be used to control the fluid flow properties of the microchannel. A single textured die can be used to produce multiple microfluidic devices making this an economical and scalable process. A flow rate increase of 186% was achieved by texturing the inner walls of a PMDS microchannel with micro bumps covered in nano bumps.

4.2   Recommendations for Future Work

1. Nano structuring to improve solar cell absorptivity can be extended to other thin film solar cell technologies such as cadmium telluride (CdTe), copper zinc tin sulfide (CZTS), dye-sensitized solar cells (DSSCs) and perovskite solar cells.

2. Further understanding of the formation mechanism of high spatial frequency LIPSS is required. This will improve the predictability of formation of nano structures for a given set of process parameters and allow simulation of LIPSS texturing processes.

3. The effects of using ARCs on LIPSS to reduce surface reflectance can be studied. Also, the effect of textured ARCs on flat silicon can be studied, which would reduce the surface recombination losses caused by increased silicon surface area.

4. Microfluidic devices with gradient hydrophobicity can be created using the process described in this work. This can be used to drive flow through microfluidic channels with the help of differences in forces of attraction without the use of external pressure.

5. The influence of superhydrophobic surfaces in heat exchangers could be studied to optimize the surface structure desirable for this application. Copper and its alloys are a good material choice for this application due to their high thermal conductivity, high formability and resistance to corrosion.

6. Multi-functional surfaces with properties such as broadband antireflection and superhydrophobicity can be studied from the standpoint of photovoltaics.

LIST OF REFERENCES

LIST OF REFERENCES

[1] M. A. Green, K. Emery, Y. Hishikawa, W. Warta and E. D. Dunlop, Solar cell efficiency tables (Version 45), Prog. Photovolt. Res. Appl. 2015, 23:1–9

[2] P. Baumgart, D.J. Krajnovich, T. A. Nguyen, A.G. Tam, A new laser texturing technique for high performance magnetic disk drives, IEEE Trans. Magn. Volume: 31, Issue: 6, Nov 1995, 2946 – 2951

[3] M. Geiger, S. Roth, W. Becker, Influence of laser-produced microstructures on the tribological behaviour of ceramics, Surf. Coat. Technol. 100-101, 1998, 17-22

[4] I. Etsion and Y. Kligerman, Analytical and Experimental Investigation of Laser-Textured Mechanical Seal Faces, Tribol. T. 42:3, 2008, 511-516

[5] G. Dumitru, V. Romano, H.P. Weber, H. Haefke, Y. Gerbig, E. Pflüger, Laser microstructuring of steel surfaces for tribological applications, Appl. Phys. A 2000, 70: 485 - 487

[6] M. Geiger, U. Popp, U. Engel, Excimer Laser Micro Texturing of Cold Forging Tool Surfaces - Influence on Tool Life, CIRP Ann. Manuf. Technol. Volume 51, Issue 1, 2002, 231-234

[7] P. Andersson, J. Koskinen, S. Varjus, Y. Gerbig, H. Haefke, S. Georgiou, B. Zhmud, W. Buss, Microlubrication effect by laser-textured steel surfaces, Wear, 262 (3–4) (2007), 369–379

[8] T. D. Ling, P. Liu, S. Xiong, et al., Surface Texturing of Drill Bits for Adhesion Reduction and Tool Life Enhancement, Tribol. Lett. (2013), 52: 113

[9] J. Bonse, R. Koter, M. Hartelt, D. Spaltmann, S. Pentzien, S. Hohm, A. Rosenfeld, J. Kruger, Femtosecond laser-induced periodic surface structures on steel and titanium alloy for tribological applications, Appl. Phys. A (2014) 117:103–110

[10] Z. Wang, C. W. Wang, M. Wang, Q. Z. Zhao, Manipulation of tribological properties of stainless steel by picosecond laser texturing and quenching, Tribol. Int. Volume 99, July 2016, 14–22

[11] A. M. Bonch-Bruevich, M. N. Libenson, V. S. Makin, and V. V. Trubaev, Surface electromagnetic waves in optics, Opt. Eng. 31, 718 (1992)

[12] T. Y. Hwang and C. Guo, Angular effects of nanostructure-covered femtosecond laser induced periodic surface structures on metals, J. Appl. Phys. 108, 073523 (2010)

[13] J. E. Sipe, J. F. Young, J. S. Preston, and H. M. van Driel, Laser-induced periodic surface structure. I. Theory, Phys. Rev. 8 Volume 27, Number 2 15 January 1983

[14] J. W. Yao, C. Y. Zhang, H. Y. Liu, Q. F. Dai, L. J. Wu, S. Lan, A. V. Gopal, V. A. Trofimov, T. M. Lysak, High spatial frequency periodic structures induced on metal surface by femtosecond laser pulses, Opt. Express Vol. 20, Issue 2, pp. 905-911 (2012)

[15] J. Bonse, A. Rosenfeld, J. Krüger, Femtosecond laser-induced periodic surface structures: recent approaches to explain their sub-wavelength periodicities, Proc. of SPIE Vol. 7994 79940M-1

[16] M. Birnbaum, Semiconductor Surface Damage Produced by Ruby Lasers, J. Appl. Phys. 36, 3688 (1965)

[17] P. M. Fauchet and A. E. Siegman, Surface ripples on silicon and gallium arsenide under picosecond laser illumination, Appl. Phys. Lett. 40, 824 (1982)

[18] X. Wang, Y.Huang, D. Liu, B. Wang, X. Zhu, and H. Zhu, Large Area Uniform Microstructures on Silicon Surface Created With a Picosecond Laser Beam Scanning, Adv. Mater. Res. Vol. 651 (2013), 327-332

[19] M.S. Trtica, B.M. Gakovic, B.B. Radak, D. Batani, T. Desai, M. Bussoli, Periodic surface structures on crystalline silicon created by 532 nm picosecond Nd:YAG laser pulses, Appl. Surf. Sci. 254 (2007), 1377–1381

[20] T. Trang D. Huynh, A. Petit, N. Semmar, Picosecond laser induced periodic surface structure on copper thin films, Appl. Surf. Sci. 302 (2014), 109–113

[21] J. Eichstädt, G.R.B.E. Römer, A.J. Huis in't Veld, Determination of irradiation parameters for laser-induced periodic surface structures, Appl. Surf. Sci. 264 (2013) 79– 87

[22] E. M. Hsu, T. H. R. Crawford, H. F. Tiedje, and H. K. Haugen, Periodic surface structures on gallium phosphide after irradiation with 150 fs – 7 ns laser pulses at 800 nm, Appl. Phys. Lett. 91, 111102 (2007)

[23] M.S. Trtica, B.M. Gakovic, B.B. Radak, D. Batani, T. Desai, M. Bussoli, Periodic surface structures on crystalline silicon created by 532 nm picosecond Nd:YAG laser pulses, Appl. Surf. Sci. 254 (2007), 1377–1381

[24] D. von der Linde, K. Sokolowski-Tinten, J. Bialkowski, Laser–solid interaction in the femtosecond time regime, Appl. Surf. Sci., 109-110, 1997, 1–10

[25] J. Bonse, R. Koter, M. Hartelt, D. Spaltmann, S. Pentzien, S. Höhm, A. Rosenfeld, J. Krüger, Tribological performance of femtosecond laser-induced periodic surface structures on titanium and a high toughness bearing steel, Appl. Surf. Sci. Volume 336, 1 May 2015, 21–27

[26] A. Y. Vorobyev and Chunlei Guo, Colorizing metals with femtosecond laser pulses, Appl. Phys. Lett. 92, 041914 (2008)

[27] B. Dusser, Z. Sagan, H. Soder, N. Faure, J.P. Colombier, M. Jourlin and E. Audouard, Controlled nanostructrures formation by ultra fast laser pulses for color marking, Opt. Express 29131, Vol. 18, No. 3 , February 2010

[28] E.B. Barmina, E. Stratakis, C. Fotakis, G.A. Shafeev, Generation of nanostructures on metals by laser ablation in liquids: new results, Quant. Electron. 40 (11) 1012 - 1020 (2010)

[29] A. B. D. Cassie and S. Baxter, Wettability of porous surfaces, Trans. Faraday Soc. 1944, 40, 546-551

[30] R. N. Wenzel, Resistance of solid surfaces to wetting by water, Ind. Eng. Chem. 1936, 28 (8), 988–994

[31] N. J. Shirtcliffe , G. McHale, S. Atherton, M. I. Newton, An introduction to superhydrophobicity, Adv. Colloid Interface Sci. 161 (2010) 124–138

[32] R. N. Wenzel, Resistance of solid surfaces to wetting by water, Ind. Eng. Chem. 1936, 28 (8), 988–994

[33] A. B. D. Cassie and S. Baxter, Wettability of porous surfaces, Trans. Faraday Soc. 1944, 40, 546-551

[34] G. McHale , N. J. Shirtcliffe and M. I. Newton, Contact-Angle Hysteresis on Super-Hydrophobic Surfaces, Langmuir, 2004, 20 (23), 10146–10149

[35] K. Ren, J. Zhou, and H. Wu, Materials for Microfluidic Chip Fabrication, Acc. Chem. Res. Vol. 46, No. 11, 2013, 2396–2406

[36] J. I. Gittleman, E. K. Sichel, H. W. Lehmann, and R. Widmer, Textured silicon: A selective absorber for solar thermal conversion, Appl. Phys. Lett. 35, 742 (1979)

[37] S. Winderbaum, O. Reinhold, F. Yun, Reactive ion etching (RIE) as a method for texturing polycrystalline silicon solar cells, Sol. Energ. Mat. Sol. Cells 46 (1997) 239-248

[38] D.H. Macdonald, A. Cuevas, M.J. Kerr, C. Samundsett, D. Ruby, S. Winderbaum, A. Leo, Texturing industrial multicrystalline silicon solar cells, Sol. Energ. 76 (2004) 277–283

[39] A.W. Smith and A. Rohatgi, A new texturing geometry for producing high efficiency solar cells with no antireflection coatings, Sol. Energ. Mat. Sol. Cells 29 (1993) 51-65

[40] J. Y. Chen, K.W. Sun, Enhancement of the light conversion efficiency of silicon solar cells by using nano-imprint anti-reflection layer, Sol. Energ. Mat. Sol. Cells 94 (2010), 629–633

[41] Y. M. Song, J. S. Yu, and Y. T. Lee, Antireflective submicrometer gratings on thin-film silicon solar cells for light-absorption enhancement, Opt. Lett. Vol. 35, No. 3, February 1, 2010, 276-278

[42] S. Sivasubramaniam, M. M. Alkaisi, Inverted nanopyramid texturing for silicon solar cells using interference lithography, Microelectron. Eng. 119 (2014) 146–150

[43] J. Oh, H. C. Yuan and H. M. Branz, An 18.2%-efficient black-silicon solar cell achieved through control of carrier recombination in nanostructures, Nat. Nanotechnol. Vol 7, November 2012, 743–748

[44] S. Liu, X. Niu, W. Shan, W. Lu, J. Zheng, Y. Li, H. Duan, W. Quan, W. Han, C. R. Wronski, D. Yang, Improvement of conversion efficiency of multi-crystalline silicon solar cells by incorporating reactive ion etching texturing, Sol. Energ. Mat. Sol. Cells 127 (2014), 21–26

[45] F. Toor, H. M. Branz, M. R. Page, K. M. Jones, and H. C. Yuan, Multi-scale surface texture to improve blue response of nanoporous black silicon solar cells, Appl. Phys. Lett. 99, 103501 (2011)

[46] H. C. Yuan, V. E. Yost, M. R. Page, P. Stradins, D. L. Meier, and H. M. Branz, Efficient black silicon solar cell with a density-graded nanoporous surface: Optical properties, performance limitations, and design rules, Appl. Phys. Lett. 95, 123501 (2009)

[47] C. H. Sun, P. Jiang, and B. Jiang, Broadband moth-eye antireflection coatings on silicon, Appl. Phys. Lett. 92, 061112 (2008)

[48] J. Zhu, C. M. Hsu, Z. Yu, S. Fan, and Y. Cui, Nanodome Solar Cells with Efficient Light Management and Self-Cleaning, Nano Lett. 2010, 10, 1979–1984

[49] A. Mavrokefalos, S. E. Han, S. Yerci, M. S. Branham, and G. Chen, Efficient Light Trapping in Inverted Nanopyramid Thin Crystalline Silicon Membranes for Solar Cell Applications, Nano Lett. 2012, 12, 2792−2796

[50] K. X. Wang, Z. Yu, V. Liu, Y. Cui, and S. Fan, Absorption Enhancement in Ultrathin Crystalline Silicon Solar Cells with Antireflection and Light-Trapping Nanocone Gratings, Nano Lett. 2012, 12, 1616−1619

[51] L. Hu and G. Chen, Analysis of Optical Absorption in Silicon Nanowire Arrays for Photovoltaic Applications, Nano Lett. vol. 7, issue 11, 2007, 3249-3252

[52] Y. Cao, A. Liu, H. Li, Y. Liu, F. Qiao, Z. Hu, Y. Sang, Fabrication of silicon wafer with ultra low reflectance by chemical etching method, Appl. Surf. Sci., Volume 257, Issue 17, 15 June 2011, 7411−7414

[53] L.A. Dobrzański, A. Drygała, K. Gołombek, P. Panek, E. Bielańska, P. Zięba, Laser surface treatment of multicrystalline silicon for enhancing optical properties, J. Mater. Process. Technol. Volume 201, Issues 1−3, 26 May 2008, 291−296

[54] X. Sedao, R. Torres, T. Sarnet, P. Delaporte and M. Sentis, Laser Textured Black Silicon Solar Cells with Improved Efficiencies, Adv. Mat. Res. Vol. 321 (2011), 240-245

[55] A.Y. Vorobyev, C. Guo, Direct creation of black silicon using femtosecond laser pulses, Appl. Surf. Sci., 257 (2011), 7291−7294

[56] T. K. Gaylord, W. E. Baird, and M. G. Moharam, Zero-reflectivity high spatial-frequency rectangular-groove dielectric surface-relief gratings, Appl. Opt. Vol. 25, No. 24, December 1986

[57] T. K. Gaylord, E. N. Glytsis, and M. G. Moharam, Zero-reflectivity homogeneous layers and high spatial frequency surface-relief gratings on lossy materials, Appl. Opt. Vol. 26, No. 15, August 1987

[58] Y. Ono, Y. Kimura, Y. Ohta, and N. Nishida, Antireflection effect in ultrahigh spatial-frequency holographic relief gratings, Appl. Opt. Vol. 26, No. 6, 15 March 1987

[59] D. H. Raguin and G. M. Morris, Analysis of antireflection-structured surfaces with continuous one-dimensional surface profiles, Appl. Opt. Vol. 32, No. 14, 10 May 1993

[60] R. C. Enger and S. K. Case, Optical elements with ultrahigh spatial-frequency surface corrugations, Appl. Opt. Vol. 22, No. 20, 15 October 1983

[61] S. Chattopadhyay, Y.F. Huang, Y.J. Jen, A. Ganguly, K.H. Chen, L.C. Chen, Anti-reflecting and photonic nanostructures, Mater. Sci. Eng. R-Rep., 69 (2010), 1–35

[62] Y. Kanamori, M. Sasaki, and K. Hane, Broadband antireflection gratings fabricated upon silicon substrates, Opt. Lett., Vol. 24, No. 20, October 15, 1999

[63] C. David, P. Haberling, M. Schnieper, J. Sochtig, C. Zschokke, Nano-structured anti-reflective surfaces replicated by hot embossing, Microelectron. Eng., 61−62 (2002) 435–440

[64] Y. Kanamori, E. Roy, Y. Chen, Antireflection sub-wavelength gratings fabricated by spin-coating replication, Microelectron. Eng. 78–79 (2005) 287–293

[65] A. Čampa, J. Krč, and M. Topič, Analysis and optimisation of microcrystalline silicon solar cells with periodic sinusoidal textured interfaces by two-dimensional optical simulations, J. Appl. Phys. 105, 083107 (2009)

[66] R. Dewan and D. Knipp, Light trapping in thin-film silicon solar cells with integrated diffraction grating, J. Appl. Phys. 106, 074901 (2009)

[67] S. Solntsev, M. Zeman, Optical modeling of thin-film silicon solar cells with submicron periodic gratings and nonconformal layers, Energy Procedia 10 (2011) 308 − 312

[68] C. Haase and H. Stiebig, Optical Properties of Thin-film Silicon Solar Cells with Grating Couplers, Prog. Photovolt: Res. Appl. 2006; 14:629–641

[69] K. R. Catchpole, A conceptual model of the diffuse transmittance of lamellar diffraction gratings on solar cells, J. Appl. Phys. 102, 013102 (2007)

[70] V. Ganapati, O. D. Miller, and E. Yablonovitch, Light Trapping Textures Designed by Electromagnetic Optimization for Subwavelength Thick Solar Cells, IEEE J. Photovolt., Vol. 4, No. 1, January 2014

[71] A. Y. Vorobyev and C. Guo, Antireflection effect of femtosecond laser-induced periodic surface structures on silicon, Opt. Express Vol. 19, Issue S5, pp. A1031-A1036 (2011)

[72] A. A. Ionin, Y. M. Klimachev, A. Y. Kozlov, et al., Direct femtosecond laser fabrication of antireflective layer on GaAs surface, Appl. Phys. B (2013) 111: 419

[73] M. H. Dar, R. Kuladeep, V. Saikiran, D. N. Rao, Femtosecond laser nanostructuring of titanium metal towards fabrication of low-reflective surfaces over broad wavelength range, Appl. Surf. Sci., Volume 371, 15 May 2016, 479–487

[74] H. Ollivier, Recherches sur la capillarité, J. Phys. Theor. Appl. 6, 757-782 (1907)

[75] D. C. Pease, The Significance of the Contact Angle in Relation to the Solid Surface, J. Phys. Chem., 1945, 49 (2), 107–110

[76] H. W. Fox, W. A. Zisman, The spreading of liquids on low energy surfaces. I. polytetrafluoroethylene, J. Colloid Sci., 5 (1950), pp. 514–531

[77] A. H. Ellison, W. A. Zisman, Wettability of Halogenated Organic Solid Surfaces, J. Phys. Chem., 1954, 58 (3), 260–265

[78] A. C. Zettlemoyer, Hydrophobic surfaces, J. Colloid Interface Sci., Vol. 28, No. 3/4, November-December 1968

[79] M. Morra, E. Occhiello, F. Garbassi, Contact angle hysteresis in oxygen plasma treated poly(tetrafluoroethylene), Langmuir, 1989, 5 (3), 872–876

[80] Z. Guo, W. Liu, B. L. Su, Superhydrophobic surfaces: From natural to biomimetic to functional, J. Colloid Interface Sci., 353 (2011) 335–355

[81] P. Roach, N. J. Shirtcliffe and M. I. Newton, Progess in superhydrophobic surface development, Soft Matter, 2008,4, 224-240

[82] B. Bhushan, Y. C. Jung, Natural and biomimetic artificial surfaces for superhydrophobicity, self-cleaning, low adhesion, and drag reduction, Prog. Mater. Sci., 56 (2011) 1–108

[83] N. A. Patankar, Mimicking the Lotus Effect: Influence of Double Roughness Structures and Slender Pillars, Langmuir 2004, 20, 8209-8213

[84] M. Nosonovsky, B. Bhushan, Hierarchical roughness optimization for biomimetic superhydrophobic surfaces, Ultramicroscopy 107 (2007) 969–979,

[85] A. Marmur, Superhydrophobic and superhygrophobic surfaces: from understanding non-wettability to design considerations, Soft Matter, 2013, 9, 7900

[86] E. Bormashenko, Progress in understanding wetting transitions on rough surfaces, Adv. Colloid Interface Sci., 222 (2015) 92–103

[87] X. Zhang, F. Shi, J. Niu, Y. Jiang and Z. Wang, Superhydrophobic surfaces: from structural control to functional application, J. Mater. Chem., 2008, 18, 621–633

[88] N. J. Shirtcliffe, G. McHale, S. Atherton, M. I. Newton, An introduction to superhydrophobicity, Adv. Colloid Interface Sci., 161 (2010) 124–138

[89] Y. Y. Yan, N. Gao, W. Barthlott, Mimicking natural superhydrophobic surfaces and grasping the wetting process: A review on recent progress in preparing superhydrophobic surfaces, Adv. Colloid Interface Sci., 169 (2011), 80–105

[90] E. Celia, T. Darmanin, E. T. de Givenchy, S. Amigoni, F. Guittard, Recent advances in designing superhydrophobic surfaces, J. Colloid Interface Sci., 402 (2013) 1–18

[91] A. M. Kietzig, S. G. Hatzikiriakos, and P. Englezos , Patterned Superhydrophobic Metallic Surfaces, Langmuir 2009, 25(8), 4821–4827

[92] M. V. Rukosuyev, J. Lee, S. J. Cho, G. Lim, M. B.G. Jun, One-step fabrication of superhydrophobic hierarchical structures by femtosecond laser ablation, Appl. Surf. Sci., Volume 313, 15 September 2014, 411–417

[93] A. Y. Vorobyev and C. Guo, Multifunctional surfaces produced by femtosecond laser pulses, J. of Appl. Phys. 117, 033103 (2015)

[94] D. V. Ta, A. Dunna, T. J. Wasleyb, R. W. Kayb, J. Stringerc, P. J. Smithc, C. Connaughtond, J. D. Shephard, Nanosecond laser textured superhydrophobic metallic surfaces and their chemical sensing applications, Appl. Surf. Sci., Volume 357, Part A, 1 December 2015, 248–254

[95] T. Baldacchini, J. E. Carey, M. Zhou, E. Mazur, Superhydrophobic Surfaces Prepared by Microstructuring of Silicon Using a Femtosecond Laser, Langmuir 2006, 22, 4917-4919

[96] B. Wu, M. Zhou, J. Li, X. Ye, G. Li, L. Cai, Superhydrophobic surfaces fabricated by microstructuring of stainless steel using a femtosecond laser, Appl. Surf. Sci., Volume 256, Issue 1, 15 October 2009, 61−66

[97] R. Jagdheesh, B. Pathiraj, E. Karatay, G. R. B. E. Romer, and A. J. Huis in't Veld, Laser-Induced Nanoscale Superhydrophobic Structures on Metal Surfaces, Langmuir 2011, 27, 8464–8469

[98] S. Moradi, S. Kamal, P. Englezos and S. G. Hatzikiriakos, Femtosecond laser irradiation of metallic surfaces: effects of laser parameters on superhydrophobicity, Nanotechnology 24 (2013) 415302

[99] S. Moradi, P. Englezos, and S. G. Hatzikiriakos, Contact Angle Hysteresis of Non-Flattened-Top Micro/Nanostructures, Langmuir 2014, 30, 3274−3284

[100] J. Long, P. Fan, M. Zhong, H. Zhang, Y. Xie, C. Lin, Superhydrophobic and colorful copper surfaces fabricated by picosecond laser induced periodic nanostructures, Appl. Surf. Sci., 311 (2014) 461–467

[101] L. Ji, X. Lv, Y. Wu, Z. Lin, and Y. Jiang, Hydrophobic light-trapping structures fabricated on silicon surfaces by picosecond laser texturing and chemical etching, J. Photon. Energy. 5(1), 053094 (Apr 07, 2015)

[102] Y. Feng, Z. Zhou, X. Ye, J. Xiong, Passive valves based on hydrophobic microfluidics, Sens. Actuators A 108 (2003) 138–143

[103] M. C. Draper, C. R. Crick, V. Orlickaite, V. A. Turek, I. P. Parkin, and J. B. Edel, Superhydrophobic Surfaces as an On-Chip Microfluidic Toolkit for Total Droplet Control, Anal. Chem. 2013, 85, 5405−541

[104] H. Andersson, W. van der Wijngaart, P. Griss, F. Niklaus, G. Stemme, Hydrophobic valves of plasma deposited octafluorocyclobutane in DRIE channels, Sensors and Actuators B: Chemical Volume 75, Issues 1–2, 30 April 2001, 136–141

[105] O. I. Vinogradova and A. L. Dubov, Superhydrophobic textures for microfluidics, Focus Article, Mendeleev Commun., 2012, 22, 229–236

[106] A. Tropmann, L. Tanguy, P. Koltay, R. Zengerle, and L. Riegger, Completely Superhydrophobic PDMS Surfaces for Microfluidics, Langmuir, 2012, 28 (22), 8292–8295

[107] K. Biernat, A. Malinowski and M. Gnat (2013). The Possibility of Future Biofuels Production Using Waste Carbon Dioxide and Solar Energy, Biofuels - Economy, Environment and Sustainability, Prof. Zhen Fang (Ed.), InTech

[108] Courtesy of Vicphysics Teachers' Network, "Spectrum,", http://www.vicphysics.org/documents/events/stav2005/spectrum.JPG

[109] H. Bao and X. Ruan, Optical absorption enhancement in disordered vertical silicon nanowire arrays for photovoltaic applications, Opt. Lett. Vol. 35, No. 20, October 15, 2010

[110] S. Oh, S. Chhajed, D. Poxson, J. Cho, E. Schubert, S. Tark, D. Kim, and J. Kim, Enhanced broadband and omni-directional performance of polycrystalline Si solar cells by using discrete multilayer antireflection coatings, Opt. Express 21, A157-A166 (2013).

[111] Courtesy of National Renewable Energy Laboratory (NREL), Golden, CO, http://www.nrel.gov/pv/copper-indium-gallium-diselenide-solar-cells.html

[112] Courtesy of National Renewable Energy Laboratory (NREL), Golden, CO, https://en.wikipedia.org/wiki/File:CIGSdevice.JPG

[113] A. Y. Vorobyev and C. Guo, Antireflection effect of femtosecond laser-induced periodic surface structures on silicon, Opt. Express A1036, Vol. 19, No. S5, 12 September 2011

APPENDIX

APPENDIX

Some additional surface textures made on copper are shown below.

1) Micro-protrusions:

   a. Without overlap

   Micro protrusions were made on copper using single pulses at a fluence of

   17 J/cm^2. A scan speed of 20 mm/s was used to prevent overlapping. Grids

   with a line spacing of 20 µm, 30 µm and 40 µm were used and the

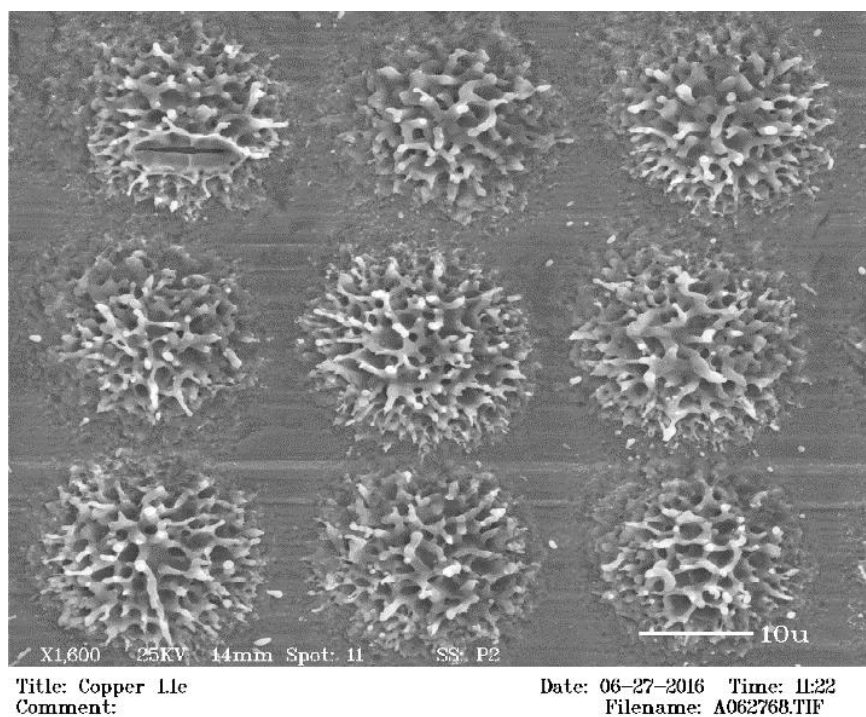   resultant structures are shown below in Figure A-1.

Figure A- 1. Micro protrusions without overlap made on the surface of copper.

b. With overlap

Next, micro protrusions were made on copper using single pulses at a fluence of 17 J/cm^2 using scan speeds of 10 mm/s and 5 mm/s. This resulted in an overlapping ratio of 67% and 83% respectively. These protrusions were distributed in grids with a line spacing of 30 µm and 50 µm and the resultant structures are shown in Figure A-2.
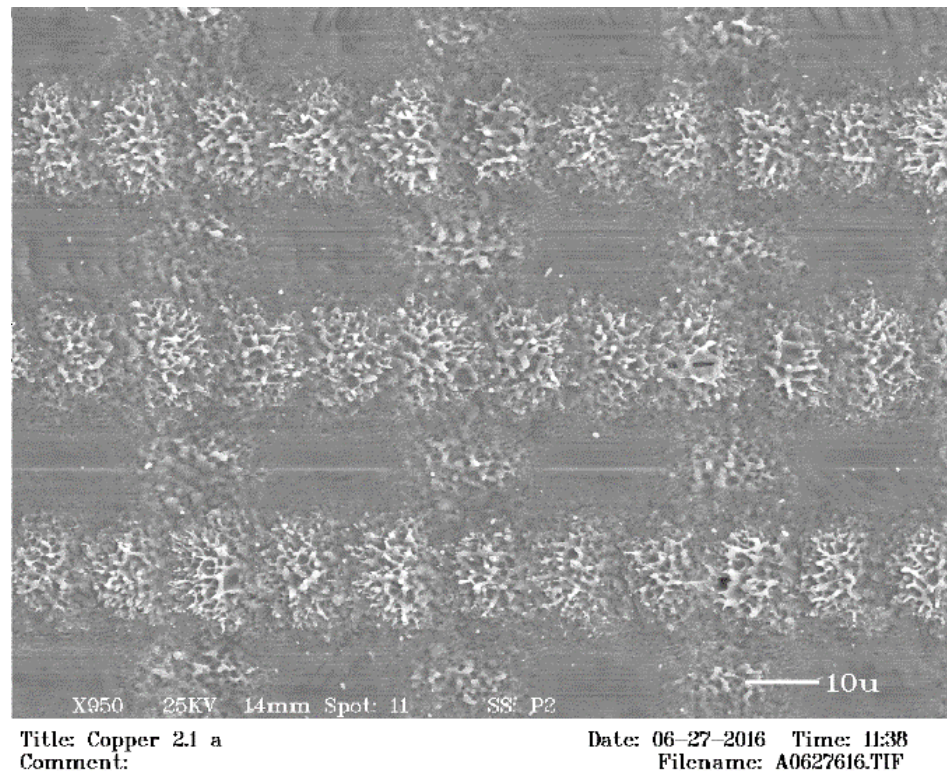

Figure A- 2. Micro protrusions with overlap made on the surface of copper.

2) Micro-protrusions and LIPSS

a. With overlap

LIPSS were created on copper at a fluence below 2 J/cm^2. Protrusions were made over this surface at 10 mm/s as seen in Figure A-3.

Title: Copper 3.1c
Comment:

Date: 06 27 2016   Time: 12:17
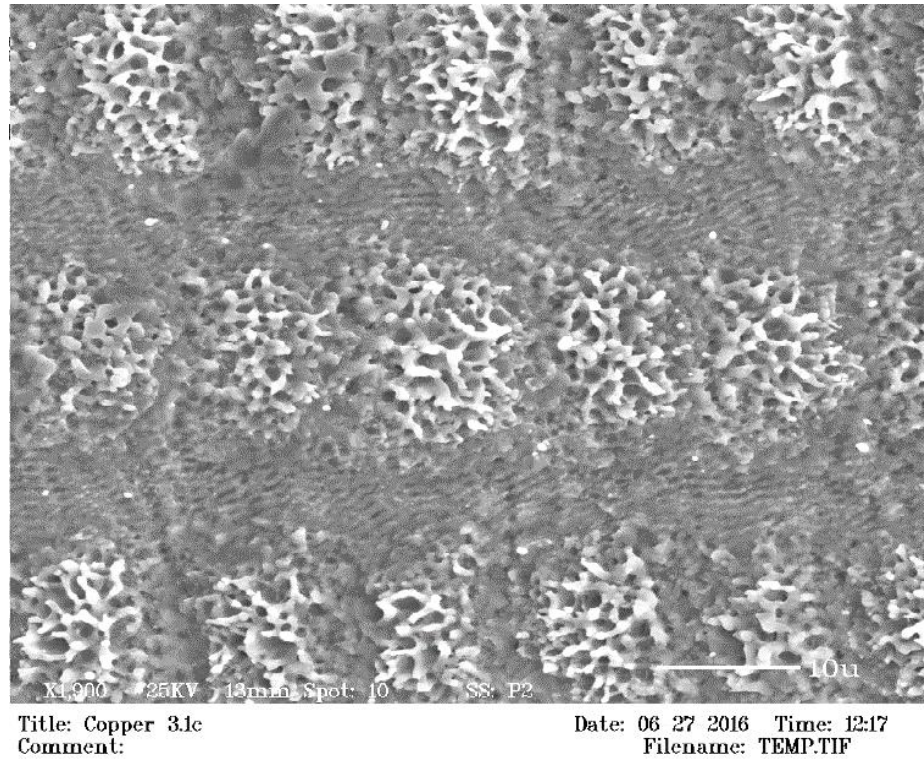Filename: TEMP.TIF

Figure A- 3. Micro protrusions with overlap and LIPSS made on the surface of copper.

    b. Without overlap

        The surface was initially covered with LIPSS formed at a fluence of 10

        J/cm^2 above which micro protrusions were formed with the same

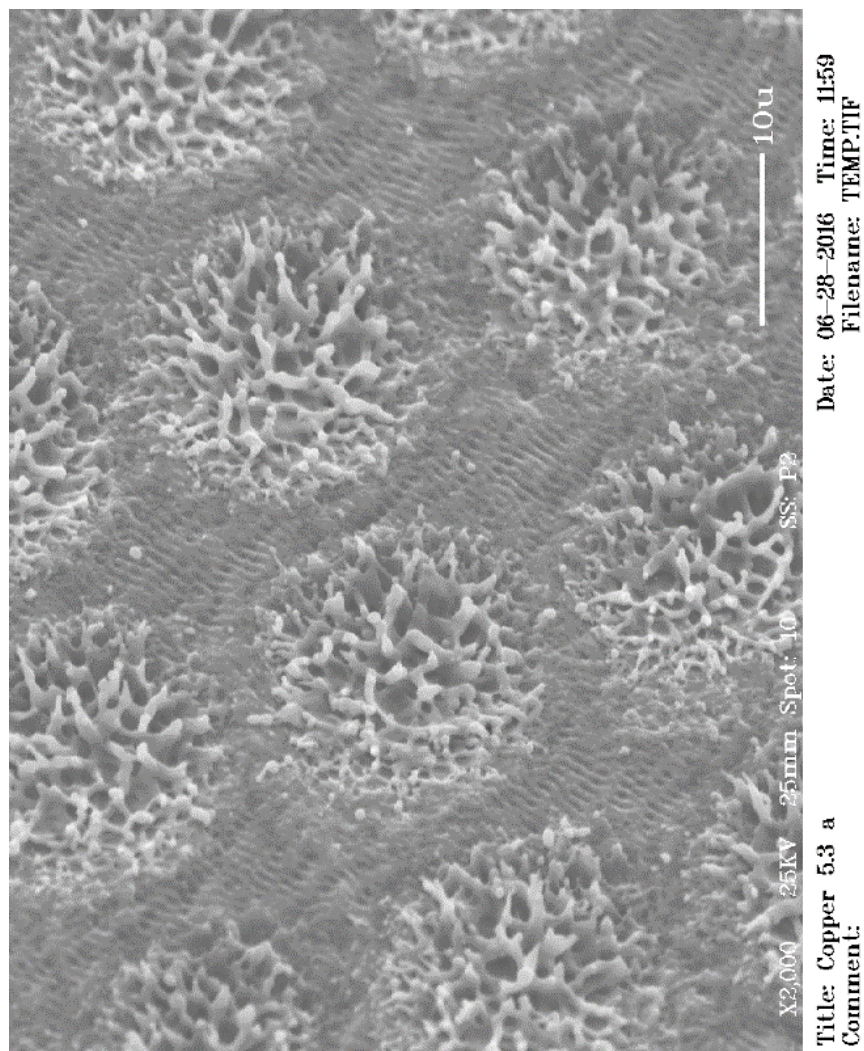   parameters as in case 1b. This is seen is Figure A-4.

Figure A- 4. Micro protrusions without overlap and LIPSS made on the surface of copper.

In all the cases discussed, the contact angle for copper ranged between 110° and 130°. The PDMS surface created by transferring the features made on copper exhibited contact angle values in the range of 120° and 135°.

VITA

VITA

Shashank Sarbada was born in Hyderabad, India. He graduated from Manipal Institute of Technology (Manipal, India) with a B.E degree in Mechanical Engineering in 2014. He began his Master of Science in Mechanical Engineering at Purdue University in August 2014. His research under the guidance of Dr. Yung C. Shin is in the field of ultra-short pulse laser surface modification and micromachining.

LIST OF PUBLICATIONS

LIST OF PUBLICATIONS

[1] S. Shashank, Z. Huang, Y. C. Shin, X. Ruan, Low-reflectance laser-induced surface nanostructures created with a picosecond laser, Phys. A (2016) 122: 45

[2] S. Shashank, Y. C. Shin, Superhydrophobic metal and polymer surfaces created using a femtosecond laser, Appl. Surf. Sci. (Submitted)